Observations of phase and intensity fluctuations for low-frequency, long-range transmissions in the Philippine Sea and comparisons to path-integral theory

John A. Colosi, Bruce D. Cornuelle, Matthew A. Dzieciuch, Peter F. Worcester, and Tarun K. Chandrayadula

Citation: The Journal of the Acoustical Society of America **146**, 567 (2019); doi: 10.1121/1.5118252
View online: https://doi.org/10.1121/1.5118252
View Table of Contents: https://asa.scitation.org/toc/jas/146/1
Published by the Acoustical Society of America

Observations of phase and intensity fluctuations for low-frequency, long-range transmissions in the Philippine Sea and comparisons to path-integral theory

John A. Colosi,[1,a)] Bruce D. Cornuelle,[2] Matthew A. Dzieciuch,[2] Peter F. Worcester,[2] and Tarun K. Chandrayadula[3]

[1]*Department of Oceanography, Naval Postgraduate School, Monterey, California 93943, USA*
[2]*Scripps Institution of Oceanography, University of California San Diego, La Jolla, California 92093, USA*
[3]*Indian Institute of Technology Madras, Chennai 600036, India*

(Received 12 April 2019; revised 28 June 2019; accepted 2 July 2019; published online 29 July 2019)

In the Philippine Sea, from April 2010 to March 2011, a 330-km radius pentagonal acoustic transceiver array with a sixth transceiver in the center transmitted broadband signals with center frequencies between 172 and 275 Hz and 100 Hz bandwidth eight times a day every other day. The signals were recorded on a large-aperture vertical-line array located near the center of the pentagon at ranges of 129, 210, 224, 379, 396, and 450 km. The acoustic arrival structures are interpretable in terms of ray paths. Depth and time variability of the acoustic observations are analyzed for six ray paths (one from each transceiver) with similar vertical sampling properties in the main thermocline. Acoustic-field statistics treated include: (1) variances of phase and intensity, (2) vertical coherence and intensity covariance, (3) glinting and fadeout rates, and (4) intensity probability density functions. Several observed statistics are compared to predictions using Feynman path-integral theory assuming the Garrett-Munk internal-wave spectrum. *In situ* oceanographic observations support this assumption and are used to estimate spectral parameters. Data and theory differ at most by a factor of two and reveal the wave propagation regimes of unsaturated, partially saturated, and fully saturated. Improvements to the evaluation of path-integral quantities are discussed.
https://doi.org/10.1121/1.5118252

[TFD] Pages: 567–585

I. INTRODUCTION

Since the 1940s discovery of the sound channel (Brekhovskikh, 1949; Ewing and Worzel, 1948), it has been known that acoustic transmissions in the ocean exhibit fluctuations in both amplitude and phase over time scales of minutes to hours, and spatial scales of meters to hundreds of meters (Eckart and Carhart, 1950). In the 1970s, a significant advancement occurred when a first order description of ocean fine structure (internal waves) was provided (Garrett and Munk, 1972); this model was integrated into weak fluctuation theory (Munk and Zachariasen, 1976), and a few experiments with controlled electronic sources, mostly at short range and mid-frequency, showed adequate agreement with the weak fluctuation theory. Buoyed by this success, coupled mode (Dozier and Tappert, 1978), moment equation (Uscinski, 1982), and Feynman path-integral (Flatté, 1983; Flatté *et al.*, 1979) techniques were developed to deal with stronger fluctuations and randomization, and a few additional field efforts similar to the earlier ones were carried out with the explicit goal of testing the new theories (Colosi, 2016). One can summarize this period as leading to enormous theoretical development on the problem of sound propagation through the stochastic ocean, but less satisfying results associated with field validation. The objective of this paper is to contribute to the field validation literature by focusing on the path integral-method for comparisons to observations in which identifiable acoustic paths are present.

While the basic principles and results from the path-integral method have been known since the 1980s (Dashen *et al.*, 1985; Esswein and Flatté, 1981; Flatté *et al.*, 1987), the actual practical implementation of the theory has evolved considerably over time. Specific issues that have been addressed include the Markov approximation and ray curvature effects (Flatté and Rovner, 2000), the parabolic approximation and ray tube functions (Colosi, 2015), the form of the horizontal coherence function (Colosi, 2013), and the small-scale spectral cut offs in the internal wave spectrum (Colosi, 2015). The present work continues in this tradition by (1) giving an improved numerical scheme for evaluating ray tube functions describing ray bundle behavior that does not require the sound-speed second vertical derivative, a difficult quantity to evaluate using experimental profiles, and (2) providing an evaluation of the phase structure function that does not use the quadratic lag approximation.

These theoretical improvements and the 2010–2011 Philippine Sea data set (Worcester *et al.*, 2013) with a 330-km radius pentagonal transceiver array (Fig. 1), precisely timed and navigated moorings, large aperture vertical array, and *in situ* oceanographic observations provide an exceptional opportunity to test the theory and to broaden the observational understanding of acoustic fluctuations. These observations at hundreds of Hertz frequencies and hundreds of kilometer ranges are quite

[a)]Electronic mail: jacolosi@nps.edu

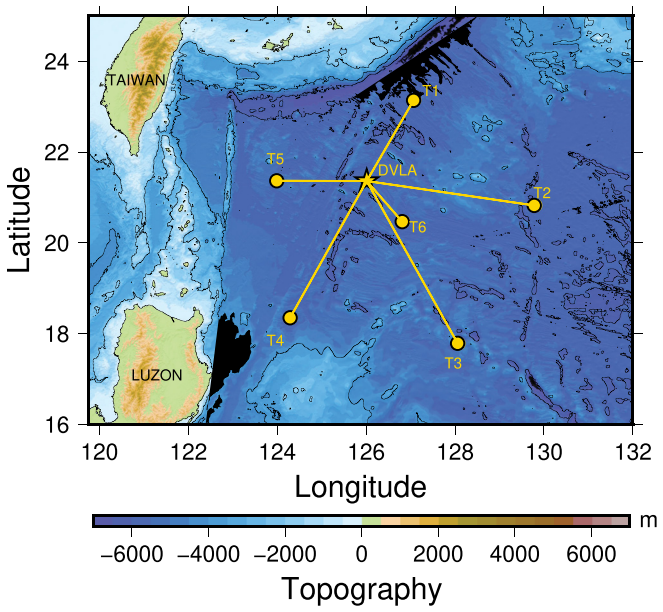

FIG. 1. (Color online) Map of the PhilSea10 experiment, showing the transmission paths analyzed in this study. Transceiver moorings forming a pentagon of radius roughly 330 km are denoted by labels T1–T6. The water-column-spanning vertical array is denoted by DVLA. See Table I for mooring details. An extensive discussion of the acoustic array can be found in Worcester *et al.* (2013).

different from earlier experiments at kilohertz frequencies and tens of kilometer ranges. Specific scientific questions to be addressed are as follows. First, the ability of path-integral equations to predict the variances of phase, intensity, and log-intensity can be evaluated. Second the large aperture vertical array makes it possible to evaluate the vertical structure of the signals using the mutual coherence function (MCF), a phase-driven observable, and the vertical intensity covariance function, an amplitude-driven observable, for comparison to path-integral predictions. Third, the aforementioned results, combined with Probability Density Functions (PDFs) of intensity and log-intensity, allow the wave propagation regimes denoted by unsaturated, partially saturated, and fully saturated acoustic field statistics to be examined (Colosi, 2016; Flatté *et al.*, 1979) and compared to predictions using the recently updated $\Lambda - \Phi$ diagram (Colosi, 2015). Fourth, with the wealth of acoustic paths oriented in many different azimuths, the assumption of horizontal isotropy in the propagation can be tested. Finally, fade-out and glint rates can be compared to multipath interference theory (Dyson *et al.*, 1976).

This paper is organized as follows. Section II gives an overview of the PhilSea 2010–2011 experiment summarizing the acoustical and oceanographic data and the data reduction methods. In Sec. III, phase fluctuation results based on acoustic travel times are presented, and an analysis of the vertical MCF is carried out. Intensity fluctuations are analyzed in Sec. IV, including moments of intensity and log-intensity, vertical intensity covariance functions, and intensity PDFs. In Sec. V, the implications of the previous results are discussed with regards to (1) wave propagation regimes, (2) form of the phase structure function, and (3) glint and fade out rates. A summary is given in Sec. VI.

II. EXPERIMENTAL DESCRIPTION

Between April 2009 and May 2011, a sequence of experiments was conducted in the western Philippine sea with multiple goals aimed at gaining a better understanding of ocean acoustics in this dynamic oceanographic region (see the experimental overview by Worcester *et al.*, 2013). In particular, there was a focus on (1) understanding acoustic propagation physics through the region's energetic fronts, eddies, internal tides, internal waves, and spice, (2) determining how acoustical and oceanographic observations can be assimilated into ocean models to provide improved predictive capability of the complex time-evolving ocean state as well as acoustic propagation conditions, (3) quantifying the spatial and temporal variability of ambient noise levels, particularly in the deep ocean below the surface conjugate depth, and (4) uncovering the seismo-acoustic physics associated with coupling between the water column sound fields and the seafloor seismic fields. In this paper, focus area (1) is addressed as it relates to sound propagation through the stochastic internal wave field.

A. Acoustics

In this study, acoustic and oceanographic observations are analyzed from a field effort carried out during an April 2010–March 2011 deployment of a 330-km radius pentagonal acoustic transceiver array (nodes T1–T6) and a nearly water-column-spanning Distributed Vertical Line Array (DVLA) receiver (Fig. 1). This array has been described in detail (Worcester *et al.*, 2013), and so only the most directly relevant aspects are presented here. In particular, the present analysis will focus on the transceiver source transmissions (T1–T6) as observed on the DVLA. These sources operated at a variety of frequencies between 172 and 275 Hz and were at distances between 129 and 450 km from the DVLA (Table I). All sources transmitted linear frequency modulated (FM) sweeps lasting 135 s at a rate of eight per day every other day, and the bandwidth for five of the six sources was 100 Hz. One source, T2, was at a lower frequency than the rest and transmitted between 140 and 205 Hz. Source levels ranged between 181.9 and 185.8 dB re 1 μPa at 1 m. While the DVLA had hydrophones throughout the water column, the depth region most relevant to this analysis is around the sound channel axis (roughly 1050 m depth). The work here therefore utilized 65 hydrophones with 20-m spacing between the depths of 702 and 1981 m.

Example transmissions (Fig. 2) from the six sources show the typical deep-ocean, mid-latitude double accordion time front pattern in which the early arriving region of the signal is composed of acoustic paths with larger grazing (axial) angles and later arriving energy has smaller grazing angles (Colosi, 2016; Munk *et al.*, 1995). Note that each branch of the time front is associated with ray paths that have an identifier (ID) given by the number of ray turning points and a sign determined by whether the launch angle at the source is upward towards the surface (positive) or downward towards the seafloor (negative) (Munk *et al.*, 1995). Figure 2 labels time front branches and IDs that are analyzed in this study. These IDs all share relatively similar source launch angles (θ_0) and ray upper turning point depths (z^+) in

TABLE I. Time front information for the six analyzed ray paths, ordered vertically from shortest to longest range. The columns are (1) source name, (2) center frequency, (3) propagation range, (4) approximate initial ray angle to the center of the receiving array, (5) range of upper turning points, (6) time front ID and number of upper turning points, (7) total number of receptions and number used in the analysis with minimum SNR above 3 dB, (8) average SNR, and (9) depth range for which the analysis is carried out. All records start on 25 April 2010 and end on 13 March 2011, except the T6 record, which ended early on 22 October 2010. Further details on the acoustic array have been published (Worcester *et al.*, 2013).

Source	f_c (Hz)	Range (km)	θ_0 (deg.)	z^+ (m)	ID/N_{utp}	Total/$N(ID)$	Ave SNR (dB)	Depth Range (m)
T6	250	129.355	−9.7	415–460	−5/2	732/703	40.9	802–1881
T5	255	210.055	10.8	370–400	9/5	1303/1203	31.1	702–1580
T1	250	224.844	12.0	290–320	9/5	1296/1146	28.6	802–1881
T4	275	379.080	11.8	315–330	15/8	1349/879	23.0	802–1781
T2	172.5	395.938	10.9	370–390	16/8	1310/954	22.0	1280–1981
T3	275	450.131	10.5	395–410	19/10	1294/792	23.1	702–1480

the main thermocline (Table I). The focus of this study is therefore limited in the sense that the fluctuations are only analyzed for a small subset of the acoustic ray paths. It will be left to subsequent studies to examine how the fluctuations vary for a wider set of acoustic ray paths. Table I shows that of the six paths analyzed, two pairs are relatively similar, that is T1 and T5, with IDs of +9 and ranges of 224 and 210 km, and T2 and T4 with IDs of +16 and +15 and ranges of 379 and 395 km. Importantly, IDs +16 and +15 both have eight upper turning points. The signal-to-noise ratio (SNR) for these six ray paths are exceptional, but a minimum SNR of 3 dB is required for the data to be included in the analysis (Table I).

The path integral analysis of the full field fluctuations requires the establishment of the mean pulse, and Fig. 3 shows the ensemble-averaged pulse computed with an overall wander removed. Consider the intensity record given by $I(z, \tau, t_j, ID)$, as a function of depth z, fast time τ, geophysical time t_j, and time front branch ID. The wavefront branch pulse travel time at a reference depth, z_r, for geophysical time, and ID is labeled $\tau_b(t_j, ID)$ and is obtained using established beamforming methodologies for ocean acoustic

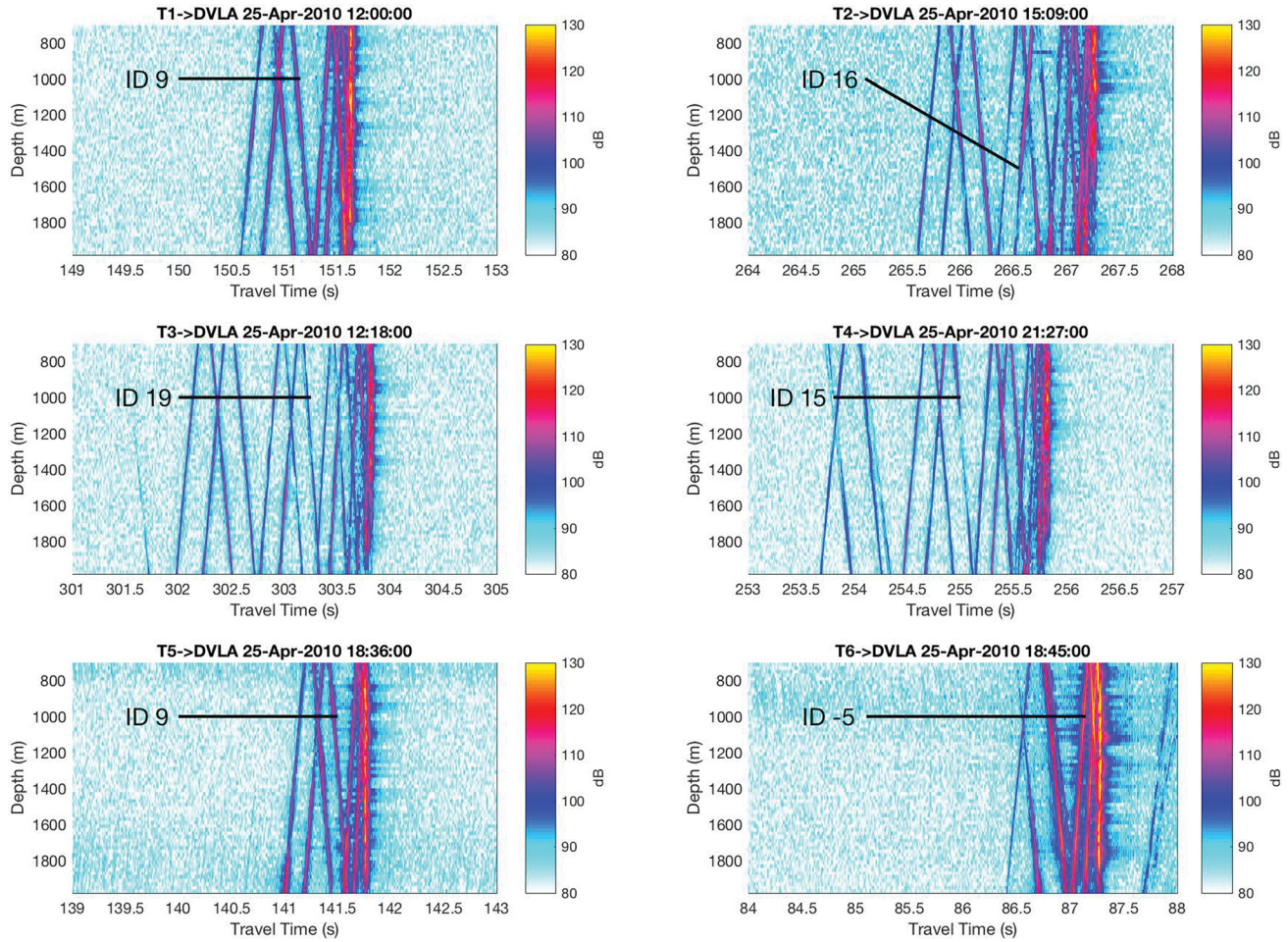

FIG. 2. (Color online) Examples of observed time fronts for transmissions from the T-moorings to the DVLA. Specific time front branches analyzed in this work are denoted with their time front ID.

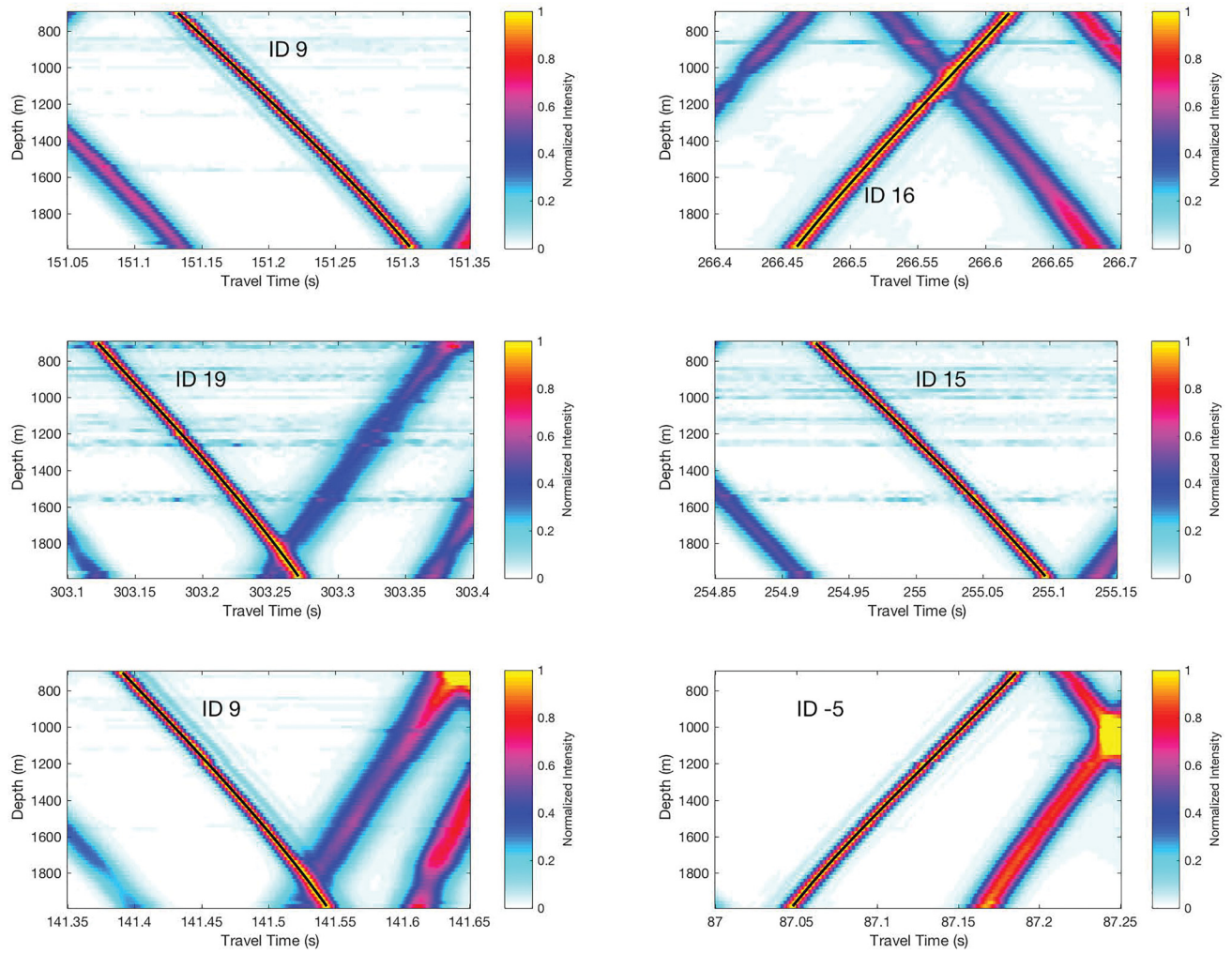

FIG. 3. (Color online) Wander-corrected mean time fronts for the six time front branches analyzed in this work. The ordering of the panels is the same as in Fig. 2. The mean time front curve, $\tau_p(z, ID)$, is shown in each panel with a black line.

tomography (Dzieciuch, 2014). The statistics of τ_b will be discussed in Sec. III. Specifically, the wander corrected mean pulse is formed by computing

$$\langle I(z,\tau,ID)\rangle = \frac{1}{N(ID)}\sum_{j=1}^{N(ID)} I(z,\tau+\delta\tau_j(t_j,ID),t_j,ID), \tag{1}$$

where the sum is over times t_j, but with a time front offset $\delta\tau_j$ that removes the large-scale pulse travel time wander of the front, τ_b, that is mostly caused by eddies and internal tides (see Sec. III.) The location of the peak of $\langle I(z,\tau,ID)\rangle$ along the array defines a mean time front shape $\tau_p(z,ID)$ that is used to extract acoustic field information along the direction of the mean front. An example of the data so processed is shown in Fig. 4. In the panels to the left, the arrival intensity is time shifted (using τ_p) to line up along the $\tau = 0$ line. Extracting the amplitude and phase (unwrapped) of the complex demodulates along the $\tau = 0$ line gives the data in the middle and right panels, complex $p(z,t_j,ID)$. Fades, glints, and phase fluctuations are evident, as seen in other vertical array studies (Duda *et al.*, 1992; Duda and Bowlin, 1994). A second method of obtaining the complex field is to perform a short-time Fourier Transform around the $\tau = 0$ line, yielding a narrowband estimate. Fluctuation statistics computed using these two methods yield nearly identical results, and therefore results using the first method are only presented here. There are depth regions for the various time front branches in which neighboring branches either cross or come close to the branch being analyzed. The depth region of analysis for each branch is reduced from the full aperture to avoid these regions (Table I and Fig. 4).

B. Ocean and sound speed structure

In this work, two oceanographic data sets are used to aid in the analysis, that is moored temperature, conductivity, depth (CTD) observations on the DVLA, and full-water-column shipboard CTDs obtained at the mooring sites during deployment and recovery. The moored observations are useful for characterizing the internal-wave spectral parameters associated with the Garrett-Munk (GM) model. The DVLA moored observations consisted of thirteen Sea bird pumped microcats (SBE37-SMP) placed between the depths of 150 and 575 m and were recording CTD observations every 4 min (Fig. 5). The upper seven instruments were 30-m apart and the remaining deeper sensors were separated by 40-m.

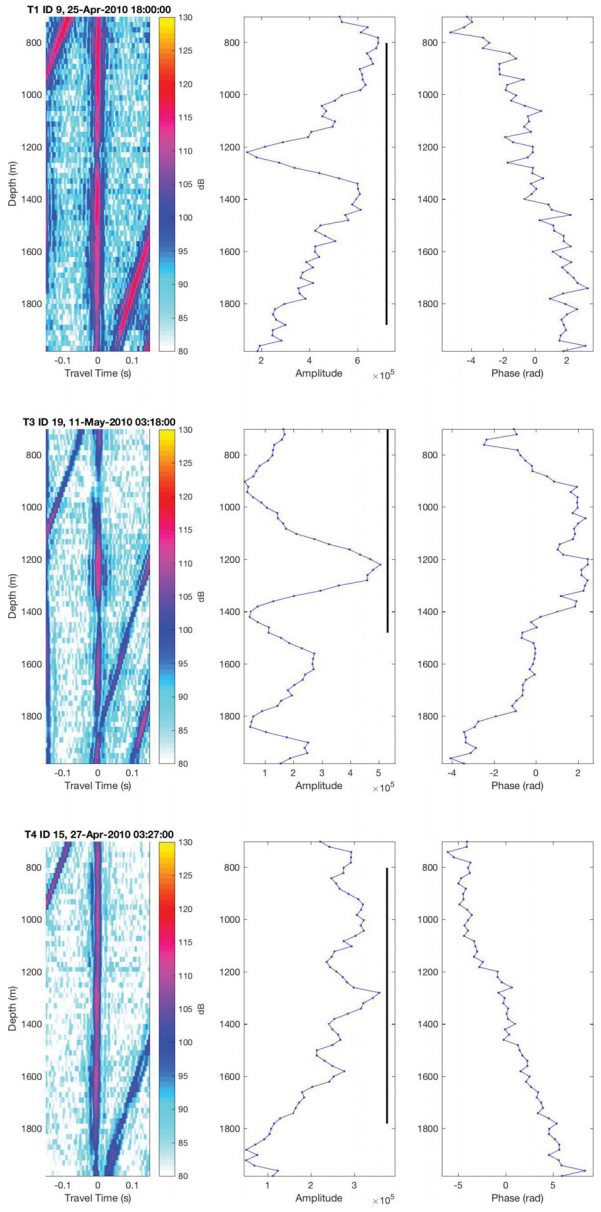

FIG. 4. (Color online) Examples of individual time fronts for transmissions from T1 (top), T3 (middle), and T4 (bottom). For each T-mooring in the left panel the tilt-corrected arrival intensity using $\tau_p(z, ID)$ is shown, where zero time corresponds to the mean time front (Fig. 3). In the middle and left panels are the amplitude and unwrapped phase at the zero time. In the middle panel, the dark vertical line corresponds to the depth region over which the analysis is carried out to avoid interference from other fronts.

Because of instrument problems, there is only good data over the depth region 150 to 600 m from 25 April 2010 to 26 July 2010. Using well established methods (Colosi *et al.*, 2012; Colosi *et al.*, 2013; DiMaggio *et al.*, 2018), the DVLA data reveal internal displacements of order from 10 to 100 m, associated with eddies, internal tides, and broadband stochastic internal waves such as described by the GM model (Fig. 5). Consistent with previous analyses (Colosi *et al.*, 2013) but not shown here, spice is weak in this depth region. Much larger spice variability is observed between the ocean surface and 150-m depth. Spectral analysis of the isopycnal displacement time series reveals an energetic field of internal waves and eddies (Fig. 6). Clear spectral lines at tidal frequencies and the associated tidal harmonics are also present (Fig. 6). The observed spectra follow the GM model for frequencies between 2 cycles per day (cpd) and several cycles per hour (cph), but there are clear discrepancies between 2 cpd and the Coriolis frequency f (Levine, 2002). Fitting a GM spectral shape to the observations in the frequency range from 6 to 24 cpd gives the root-mean-square (rms) displacement as a function of depth (Fig. 6, middle panel). This curve can be compared to a Wentzel–Kramers–Brillouin (WKB) scaled rms displacement, $\langle \zeta^2 \rangle^{1/2} = \zeta_0 \sqrt{N_0/N(z)}$ where ζ_0 is a reference displacement at the buoyancy frequency $N_0 = 3$ cph. The standard GM model has $\zeta_0 = 7.3$ m, but a better fit to the data is $\zeta_0 = 7.3 \times \sqrt{1.94} = 10.17$ m. This is nearly twice the standard GM energy.[1] For comparison, Fig. 6 also shows the rms internal tide displacements in the diurnal and semidiurnal bands obtained by least square fits using five diurnal frequencies (O1, K1, P1, Q1, and J1) and five semidiurnal frequencies (M2, S2, N2, K2, and L2). The internal tides are comparable to the GM-like internal waves in rms displacement, but the internal tide vertical structure is dominated by mode 1, while the stochastic internal waves have more high-mode energy that is important for several of the acoustic observables such as intensity variance and vertical coherence.

To characterize the background sound speed and stratification over the region to be used in theoretical calculations, fourteen full-water-column shipboard CTDs were taken at the seven mooring locations during deployments (April 2010) and recoveries (March 2011). The average profiles of temperature, salinity, potential density, buoyancy frequency, potential sound speed gradient, and sound speed in the upper ocean computed from these CTDs and from the DVLA mooring are shown in Fig. 7. The averaged moored observations are generally consistent with the ship observations. The sound channel axis is located near 1050 m depth. Importantly for the fluctuation calculations that utilize $c(z)$, $(dc/dz)_p(z)$, and $N(z)$ (Appendix A), there are large vertical scale variations in the sound speed gradient and buoyancy frequency in the depth range between 500 m and the surface where the acoustic ray paths have upper turning points.

III. TRAVEL TIME AND PHASE FLUCTUATIONS

Here, the fluctuations in time-front travel time ($\delta\tau$) are interpreted to provide critical information regarding fluctuations in phase ($\delta\phi$) using the simple relation $\delta\phi = \omega_c \delta\tau$ where ω_c is the center frequency. Examples of travel-time fluctuations obtained using established methodologies (Dzieciuch, 2014) are shown in Fig. 8. The three main components of the fluctuations are seen namely, eddies, internal tides, and random internal waves. A decomposition of the rms travel time and phase variation for the six ray paths is given in Table II.

A. Eddy and internal tide travel time fluctuations

The largest fluctuations are due to eddy or mesoscale processes (Table II). This variation is quantified by low pass filtering the travel-time time series with a cutoff frequency of 1/3 cpd. To intercompare the paths with different propagation ranges, the rms travel times are scaled using a square root rule appropriate for an isotropic mesoscale correlation

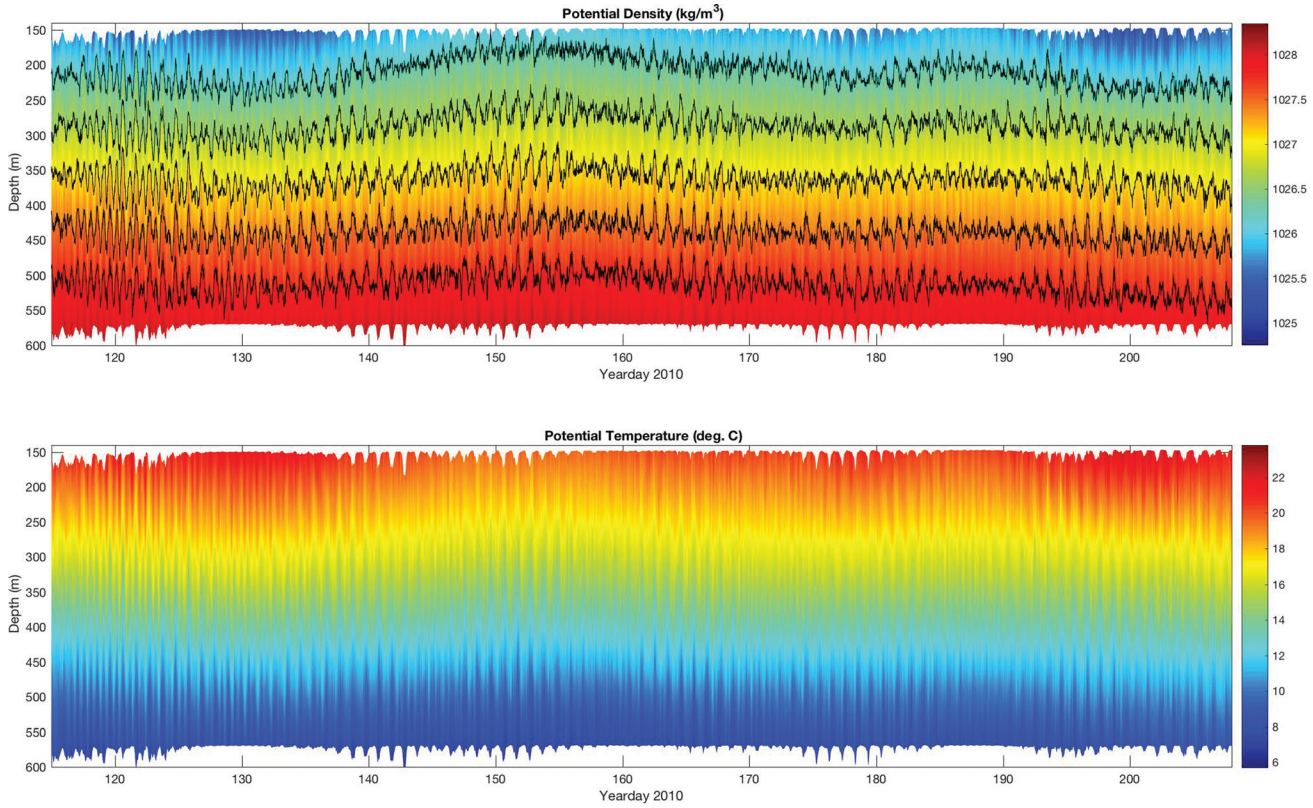

FIG. 5. Potential density (upper) and potential temperature (lower) at the DVLA as a function of depth and time. In the upper panel, the depths of a few isopycnals are shown. Because of instrument failures, the data are incomplete after yearday 208.

length shorter than the range (Colosi, 2016). In Table II, the range scaling is $\sqrt{R_0/R}$ where the reference range is $R_0 = 200$ km and R is the range of the observation. The southern paths T3, T4, and T5 have larger variations than the northern paths T1 and T2, suggesting greater eddy activity (Ramp *et al.*, 2017). The T6 path is anomalously low because the range is so short and is comparable to the eddy correlation length. Here, a scaling closer to linear with range is likely more appropriate and would reconcile the result with the other paths.

The next largest travel time fluctuations are due to the internal tide. The rms travel time is obtained by tidal fits using the five diurnal and semi-diurnal constituents described in Sec. II B. Like the mesoscale variation the internal tide fluctuations are seen to be highly anisotropic, with the largest variations on paths aligned in the North/South

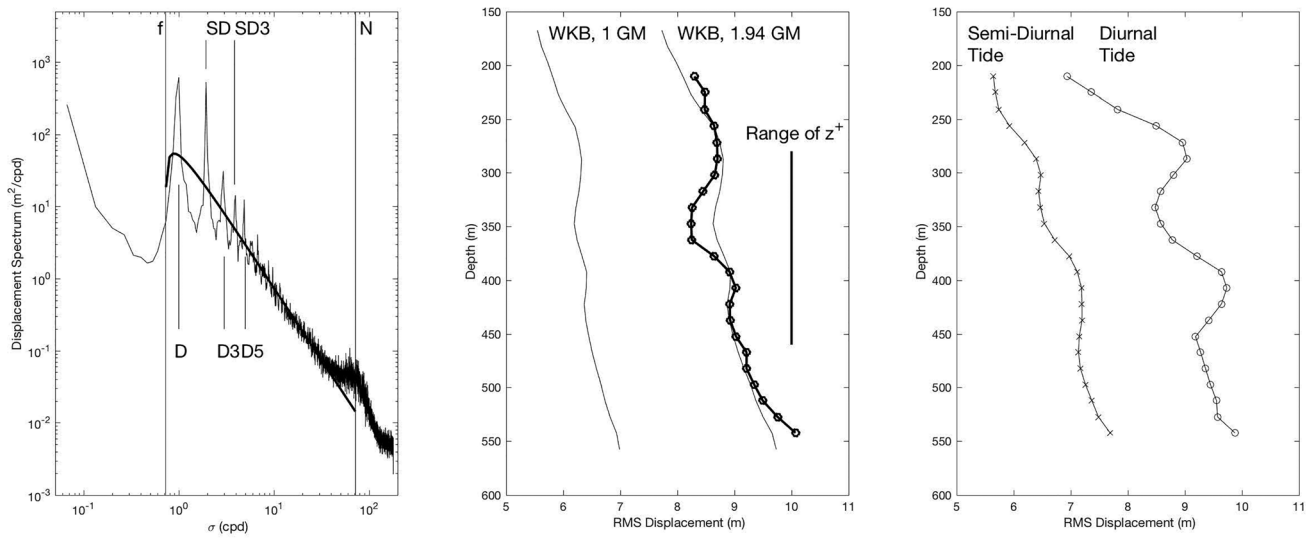

FIG. 6. Vertical isopycnal displacement spectra (left) that are averages over 23 isopycnals with mean depths between 212 and 542 meters. The bold curve shows a GM spectrum fit to the observations. The Coriolis and buoyancy frequencies are annotated with f and N, respectively. Diurnal/semidiurnal frequencies and associated harmonics are annotated with D and SD, respectively. In the center and right panels, rms displacements for stochastic internal waves (center) and internal tides (right) are shown. Light curves in the center panel show WKB estimates at the standard GM energy and a fit to the observations using 1.94 times the standard energy.

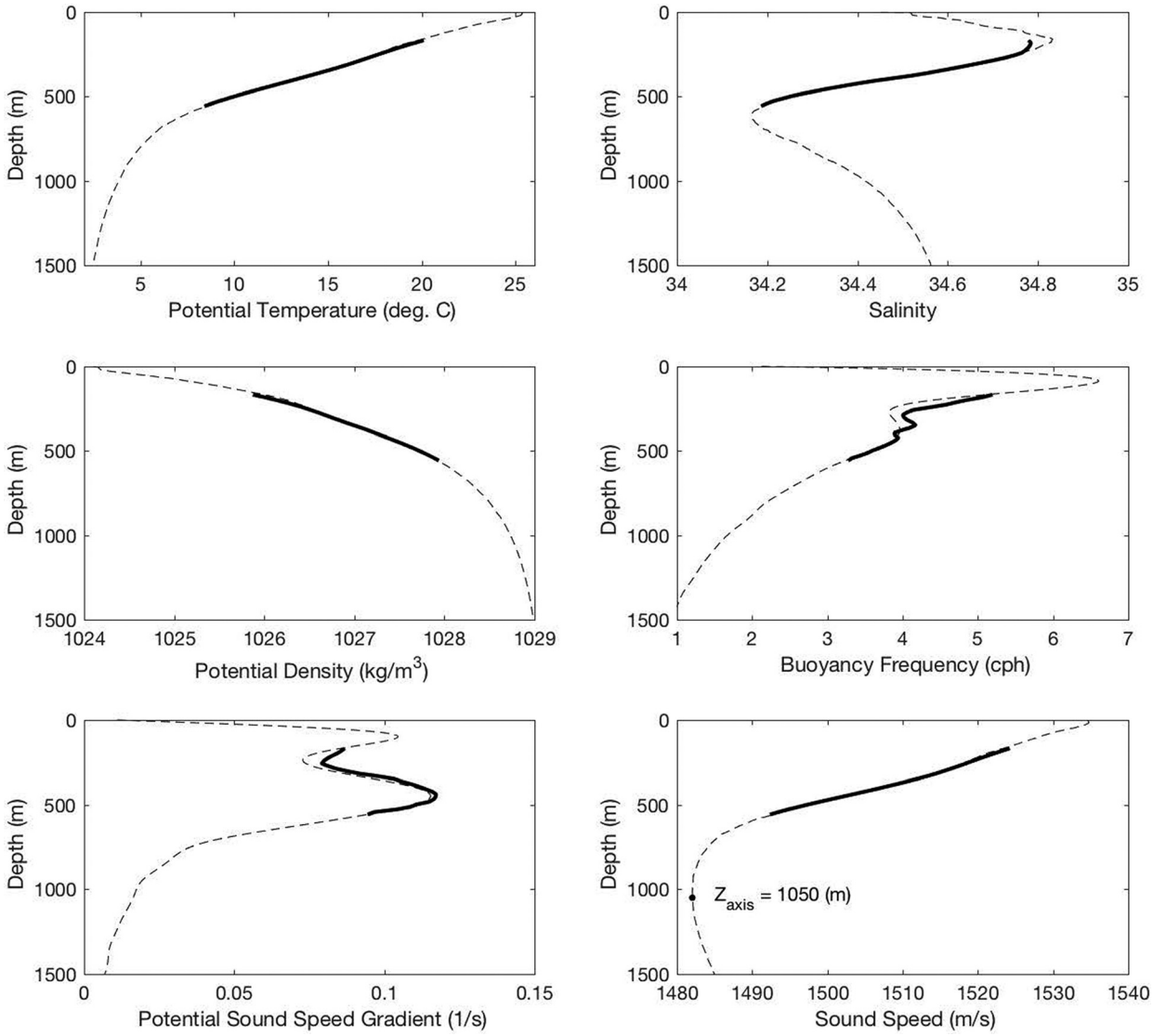

FIG. 7. Mean profiles of potential temperature, salinity, potential density, buoyancy frequency, potential sound speed gradient, and sound speed. Bold lines are from the DVLA mooring, and the thin lines are averages of CTDs taken during mooring deployment and recovery.

direction and closer to the Luzon Strait, the dominant local source of the internal tides (Kerry *et al.*, 2013; Powell *et al.*, 2013).

B. Stochastic internal wave travel time and phase fluctuations

The observation schedule of eight samples per day every other day makes quantification of the stochastic internal wave fluctuations with frequencies between 6 cph and the Coriolis frequency ($f = 0.7167$ cpd) problematic and prone to uncertainty. A time-domain approach was therefore taken. The mesoscale and tidal time series were subtracted from the raw travel times, and a travel-time autocovariance function was then computed from the high-pass records. The rapid decorrelation of the travel times from the zero to first lag (3 h) was used to estimate the stochastic internal wave contribution to the travel-time and phase variance (Table II). Specifically, the stochastic variances are estimated using the difference between the zero and first lag of the autocovariance function. As with the mesoscale and internal tide rms travel times, the internal wave values can be scaled by the square root of range. For internal wave scattering, the upper turning points are critical, so a square root scaling based on the number of upper turning points, N_{utp}, is used. The scaled values so obtained (Table II) for the different paths are similar, pointing to the fact that the internal wave scattering, unlike scattering due to mesoscale and internal tides, is relatively isotropic in the horizontal. Last, the rms phase fluctuations due to the stochastic internal wave field are seen to be significant and greater than a cycle for all paths. This large phase variability means that microray interference is possible (see Chap. 4 of Colosi, 2016).

The observed fluctuations are next compared to the well-known path integral result for the travel-time variance using the ray tangent approximation

$$\tau^2 = \int_\Gamma \frac{\langle \mu^2 \rangle L_p(\theta, z)}{c^2(z)} ds, \tag{2}$$

where Γ is the ray path, $\mu^2 = \langle \delta c^2(z) \rangle / c^2(z)$ is the fractional sound-speed variance, and $L_p(\theta, z)$ is the correlation length

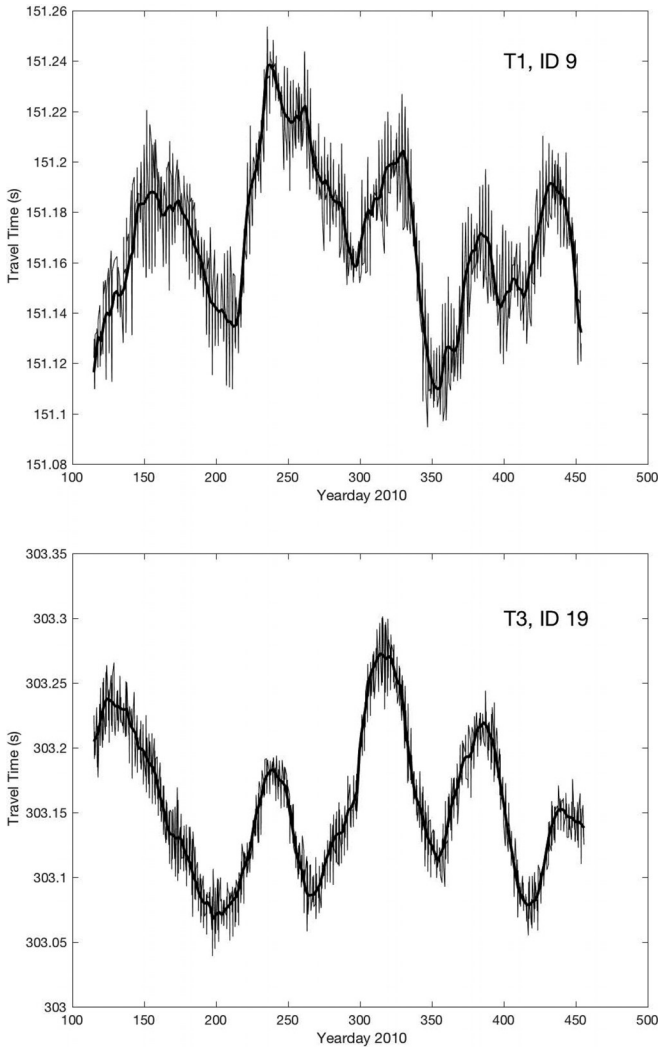

FIG. 8. Examples of travel-time time series for transmissions from moorings T1 (top) and T3 (bottom). Thin lines show raw travel times. The thick lines have been low-pass filtered with a cutoff frequency of 1/3 cycle per day in order to show fluctuations associated with mesoscale variability.

of the internal waves in the direction of the ray θ (Appendix A gives details of these functions). The phase variance is simply $\Phi^2 = \omega_c^2 \tau^2$. The theory generally under predicts the rms values, accounting for 60%–80% of the observations (Table II). This agreement, being better than a factor of two, should be considered acceptable given the uncertainties associated with the observed values (sampling) and the approximations going into the theory, including the assumption of GM internal-wave dominance.

C. Vertical mutual coherence functions

An important phase-driven observable is the vertical mutual coherence function (VMCF). This function is related to vertical beamforming performance and gives information regarding achievable coherent processing gain. To compute the VMCF, the observed complex acoustic field along the average time front, $p(z, t_j, ID)$ (Fig. 4), is normalized by the square root of the mean intensity, $\langle I(z, ID)\rangle = \langle |p(z, t_j, ID)|^2 \rangle$, to obtain the pressure field $\hat{p}(z, t_j, ID)$. The complex autocovariance of this quantity gives VMCF $(\Delta z_r, ID) = \langle \hat{p}(z_1, t_j, ID)\hat{p}^*(z_2, t_j, ID)\rangle$ where the ensemble average is over all times and pairs of depth points z_1 and z_2 with separation Δz_r. The depth range of the points going into each calculation (Table I, column 9) is limited due to interference from other time front branches (Fig. 3). The observed VMCFs are shown in Fig. 9, and the vertical coherence lengths, z_0, defined at the $e^{-1/2}$ point are given in Table II. The coherence lengths range between 88 and 218 m. The smallest value as expected is for the T3, 275-Hz, 450-km path, while the largest value is surprisingly for the T2 172.5-Hz, 396-km path. The shortest path, T6, at 250 Hz and 129 km has a slightly smaller coherence length of 182 m compared to the T2 value of 218 m. The T1 and T5 paths, similar in both frequency and range, have nearly the same coherences of 129 and 116 m, respectively.

The path integral result for the VMCF has been derived (Dashen *et al.*, 1985) and is given by

$$\langle pp^*(\Delta z_r)\rangle = \exp\left[-\frac{D(\Delta z_r)}{2}\right], \tag{3}$$

where $D(\Delta z_r)$ is the phase structure function for two paths originating at the source and ending up a distance Δz_r apart at the receiver range. Using the ray tangent approximation, the phase structure function can be written (see Chap. 7 of Colosi, 2016)

TABLE II. Travel time and phase statistics for the six analyzed ray paths, ordered vertically from shortest to longest range. Columns 2 to 4 show rms travel time due to mesoscale (τ_{MS}), internal tide (τ_{IT}), and internal wave (τ) variability. For mesoscale, internal tide, and internal waves (Columns 2, 3, and 5), range-scaled rms fluctuations are also shown, where the scaling factor is $\sqrt{R_0/R}$, with $R_0 = 200$ km the reference range and R the range of the observation (Table I). In column 5, there is also a scaling based on number of upper turning points N_{utp} given by $\sqrt{5/N_{utp}}$ (Table I). For internal waves, the rms phase fluctuations Φ are shown in column 6. The vertical coherence length z_0, or inverse phase rate, is shown in column 7, and a turning-point and frequency-scaled coherence length is shown in column 8. The frequency scaling is linear and is given by $250/f_c$, where f_c is the center frequency in Hz [Eq. (5)]. Predictions for τ and Φ (columns 4 and 6) are computed using Eq. (2).

Source	τ_{MS} (ms) obs/scaled, R	τ_{IT} (ms) obs/scaled, R	τ (ms) obs/pred	τ (ms) scaled, R/N_{utp}	Φ (rad) obs/pred	z_0 (m/rad) obs/pred	z_0 (m/rad) scaled, N_{utp} and freq.
T6	11.9/14.8	8.5/10.6	3.9 ± 1.1/2.9	4.9/6.2	6.2/4.5	182 ± 10/302	115
T5	35.9/35.1	6.8/6.6	5.9 ± 1.8/4.1	5.8/5.9	9.5/6.6	116 ± 10/176	118
T1	28.8/27.1	10.7/10.1	5.7 ± 1.7/3.8	5.4/5.7	8.9/6.0	129 ± 10/210	129
T4	52.3/38.0	22.3/16.2	8.2 ± 2.4/4.9	5.9/6.4	14.1/8.5	100 ± 10/139	139
T2	37.3/26.5	5.7/4.0	6.6 ± 2.0/5.2	4.7/5.2	7.1/5.7	218 ± 15/259	190
T3	54.5/36.3	11.6/7.8	7.9 ± 2.4/6.0	5.3/5.6	13.7/10.3	88 ± 10/106	137

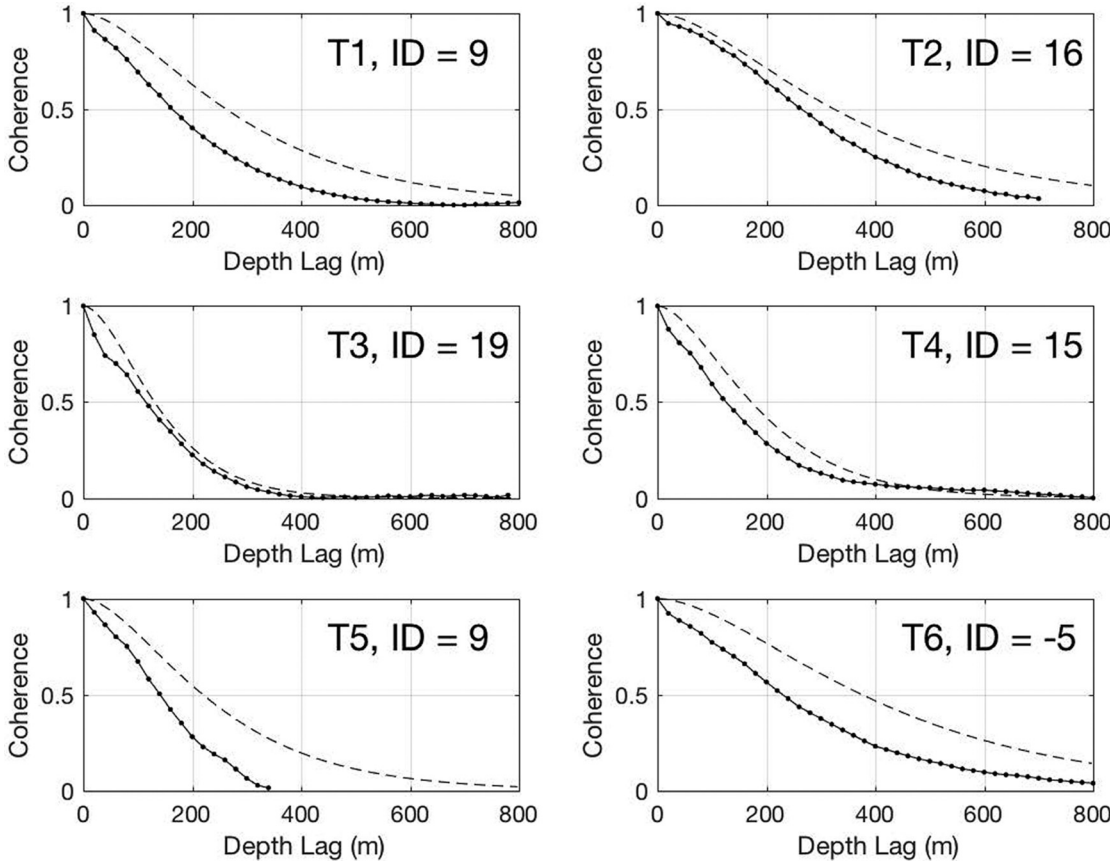

FIG. 9. Observed (dotted) and modeled (dash) vertical mutual coherence functions for the six ray paths. Vertical coherence lengths defined as the $e^{-1/2}$ point of the functions are given in Table II.

$$D(\Delta z_r) = 2\omega_c^2 \int_\Gamma \frac{\langle \mu^2 \rangle L_p(\theta, z)}{c^2(z)} \frac{1}{\langle j^{-1} \rangle} \times \sum_{j=1}^{J} H(j) \left[\frac{1 - \cos\left(m(j)\Delta z(s)\right)}{j} \right] ds, \tag{4}$$

where $H(j)$ is the internal wave vertical mode spectrum, $m(j) = \pi j N(z)/N_0 B$ is the WKB internal wave vertical wave number, and $\Delta z(s) = \xi_1(s)\Delta z_r$ is the vertical separation between the two ray paths. The factor $\xi_1(s)$ is the vertical ray tube function as described in Appendix B. What has typically been done is to Taylor expand the cosine such that $D(\Delta z_r) = \Delta z_r^2 / z_0^2$, giving an explicit expression for the correlation length, z_0

$$\frac{1}{z_0^2} = \omega_c^2 \int_\Gamma \frac{\langle \mu^2 \rangle L_p(\theta, z)}{c^2(z)} \frac{\langle j \rangle}{\langle j^{-1} \rangle} \left(\frac{\pi N(z)}{N_0 B} \right)^2 \xi_1^2(s) ds. \tag{5}$$

It is found here that for the ranges involved, the quadratic expansion is not accurate enough, and so Eq. (4) is utilized (see more discussion of this point in Sec. V B). The quadratic expansion gives estimates of the coherence length that are always smaller than those from the full equation. A comparison of observed and predicted coherence functions is given in Fig. 9. Comparing the predicted and observed coherence lengths, z_0, (Table II, column 7), in all cases the prediction is larger than the observation by 19% and 66%. As with the rms travel time observable, this theory/observation comparison, which is much better than a factor of two, is rather good given the approximations and assumptions.

Table II also shows turning point and frequency-scaled observed values of z_0. Here, the values are scaled to five upper turning points and a center frequency of 250 Hz. The values are all rather close, suggesting, as was seen in the travel time fluctuations, that the propagation is roughly isotropic in the horizontal.

IV. INTENSITY FLUCTUATIONS

The Philippine Sea receptions show a broad range of fade-out and scintillation behavior (Fig. 10) that are quantified here using moments, the vertical covariance function, and Probability Density Functions (PDFs). From Fig. 10, it is seen that the glinting or high intensity behavior is localized in space, and given our coarse time sampling, temporally intermittent. Indeed, the time scale of the intensity fluctuations computed using the time lagged intensity correlation function (not shown) is on the order of or shorter than the minimum sample separation (3 h) with no significant modulation at tidal or mesoscale frequencies. Therefore, each point in the intensity time series can be considered to be an independent sample of the variability. The lack of tidal modulation for the paths analyzed here does not support the proposal of White *et al.* (2016), who suggest that internal tide deformation of the background sound-speed profile can lead to a shifting of the large-scale turning-point caustic

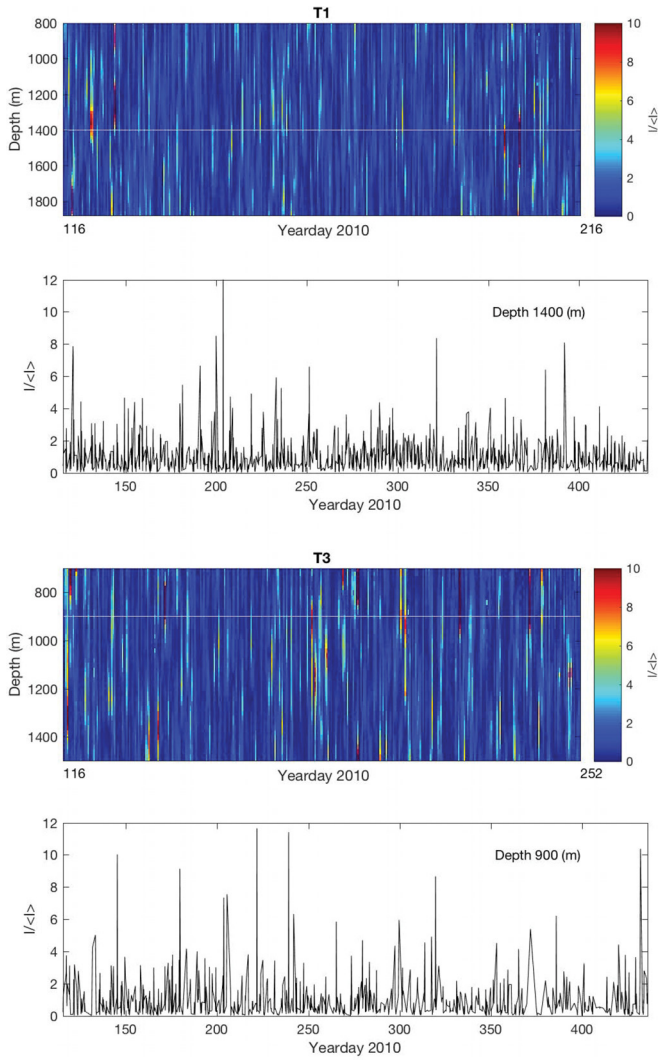

FIG. 10. (Color online) Examples of unit mean intensity along the timefront at the DVLA as a function of depth and time for the transmissions from moorings T1 (top two) and T3 (bottom two). The color panels show a limited time range so that the scintillations are more evident. The line plots show the complete time record at 1400 and 900 m for T1 and T3, respectively.

structure, thereby causing tidal period intensity fluctuations for receivers quite distant from the turning points. For the ray paths examined here, it appears that scattering mechanisms associated with the diffuse stochastic internal-wave field are likely dominant.

A. Intensity moments

An observable that quantifies the glinting behavior is the scintillation index

$$SI = \frac{\langle I^2\rangle - \langle I\rangle^2}{\langle I\rangle^2}. \tag{6}$$

A second observable that is more sensitive to fade out behavior is the variance of log-intensity

$$\sigma^2_{\ln I} = \langle(\ln I)^2\rangle - \langle(\ln I)\rangle^2. \tag{7}$$

Table III shows estimates of these moments from the observations. As expected, the shortest path, T6, shows the least fluctuation with values much less than 1. The common paths, T1 and T5 show similar fluctuations. The other common paths, T2 and T4, but with different frequencies, show as expected more fluctuation at the higher frequency. These results suggest a degree of isotropy. The longest path, T3, shows the most variability, indicating that the fluctuations may continue to grow with range before they start decreasing on their way to saturation (Colosi, 2016, see Sec. V A).

In weak fluctuation theory, the variance of log-intensity is given by

$$\sigma^2_{\ln I} = 2\omega_c^2 \int_\Gamma \frac{\langle\mu^2\rangle L_p(\theta,z)}{c^2(z)} \frac{1}{\langle j^{-1}\rangle} \times \sum_{j=1}^{J} \frac{H(j)}{j}\left[1-\cos\left(\frac{m^2(j)R_f^2(s))}{2\pi}\right)\right] ds, \tag{8}$$

where $R_f^2(s)$ is the vertical Fresnel Zone (Colosi, 2016, and Appendix A). If the log-intensity has a normal distribution, then

$$SI = \exp(\sigma^2_{\ln I}) - 1 \simeq \sigma^2_{\ln I}, \tag{9}$$

a result that will be used to obtain crude predictions of SI. These weak fluctuation results are only expected to apply in the unsaturated propagation regime where $\sigma^2_{\ln I} < 1$. Indeed, in Table III these estimates only show reasonable agreement for the T1, T5, and T6 paths that have shortest ranges. The longer-range, low-frequency path, T2 is marginally in agreement, while the T3 and T4 paths are widely off.

TABLE III. Intensity statistics for the six analyzed ray paths, ordered vertically from shortest to longest range. In columns 2 and 3, the diffraction parameter Λ and the product $\Lambda\Phi^2$ are shown to indicate wave propagation regime (column 9). Columns 4 to 6 give observed and predicted scintillation index, rms of log-intensity, and vertical correlation length of intensity. The glint and fade-out rates R_g and R_d are derived from the data using glint and fadeout thresholds of +6 dB and −10 dB relative to the mean intensity. In column 9, the abbreviations correspond to US = Unsaturated, PS = Partially Saturated, and S = Saturated.

Source	Λ	$\Lambda\Phi^2$	SI obs/pred	$\sigma_{\ln I}$ obs/pred	z_I (m/rad) obs/pred	R_g (hr phone)$^{-1}$	R_d (hr phone)$^{-1}$ obs/pred	Regime
T6	0.0594	1.20	0.29 ± 0.01/0.32	0.59 ± 0.04/0.57	131 ± 10/193	0.025	0.080/0.71	US
T5	0.0825	3.60	0.97 ± 0.10/0.93	1.09 ± 0.03/0.96	128 ± 10/113	0.52	0.91/1.16	US/PS Border
T1	0.136	4.95	0.96 ± 0.11/1.16	1.09 ± 0.04/1.08	147 ± 10/134	0.51	1.04/1.13	PS
T4	0.186	13.4	1.52 ± 0.13/2.94	1.17 ± 0.04/1.71	147 ± 10/90	0.89	1.16/1.58	PS
T2	0.254	8.16	0.95 ± 0.07/1.71	1.02 ± 0.02/1.31	183 ± 15/164	0.61	0.71/0.99	US/S Border
T3	0.141	15.0	1.56 ± 0.28/3.50	1.20 ± 0.05/1.87	122 ± 10/70	0.98	1.22/1.76	PS

B. Intensity covariance function

Figure 10 suggests the vertical spatial scale of the intensity variability is of order a hundred meters. To compute the vertical intensity covariance function, a unit mean intensity normalization is used ($\langle I \rangle = 1$). The intensity covariance function is then given by

$$\langle I_1(z_1) I_2(z_2) \rangle = \langle I_1 I_2(\Delta z_r) \rangle, \tag{10}$$

and should asymptote to one at large separations. In both the fully saturated and partially saturated regimes, the path integral result is quite simple, yielding (Colosi, 2016)

$$\langle I(\Delta z_r) I \rangle = 1 + SI \exp\left[-D(\Delta z_r)\right]. \tag{11}$$

As with the vertical mutual coherence formula, the key term here is the phase structure function, $D(\Delta z_r)$. Defining the vertical intensity correlation length, z_I, as the $e^{-1/2}$ decay scale, it is found that z_0 and z_I are closely related. In fact, if the structure function were quadratic in lag, then the relation would be $z_I = z_0/\sqrt{2}$, but this is not precisely the case (Sec. V B).

Comparisons between observed and predicted intensity covariance functions are shown in Fig. 11, and intensity correlation scales are given in Table III. The observed correlation scales vary in a rather narrow region between 122 and 183 m, while the theory varies between 70 and 193 m. As with the vertical MCF observations, the smallest correlation length is for the longest path, T3, and the largest correlation length is for the low-frequency path, T2. Theory correctly predicts the smallest correlation length to be T3, but the largest length is predicted to be for T6, with T2 coming in a close second. Theory and observation are in excellent agreement for the two similar paths T1 and T5 as well as for T2. The agreement is less satisfactory for the other paths, but is still well within a factor of two.

C. PDFs

Observed PDFs of log-intensity and intensity are shown in Figs. 12 and 13 together with exponential and log-normal model distributions. The log-intensity distributions provide insight into fade-out behavior. For all paths, a significant number of fade-outs are observed that are 4 to 5 times the standard deviation. The low intensity side of the PDFs roughly follow the exponential distribution, indicating the importance of interference.[2] The paths T2, T3, and T4 have lower SNR than the other three paths (Table I), so the low intensities are not as well sampled. On the high end of the log-PDFs, the observations generally fall between the exponential and log-normal distributions, although the high intensity region is better observed using the linear intensity PDFs. It is somewhat of a surprise that the T6 PDF does not more closely resemble a log-normal given that the log-intensity variance is rather small.

The linear intensity PDFs reveal remarkable glinting behavior, with some paths showing focusing up to 14 times

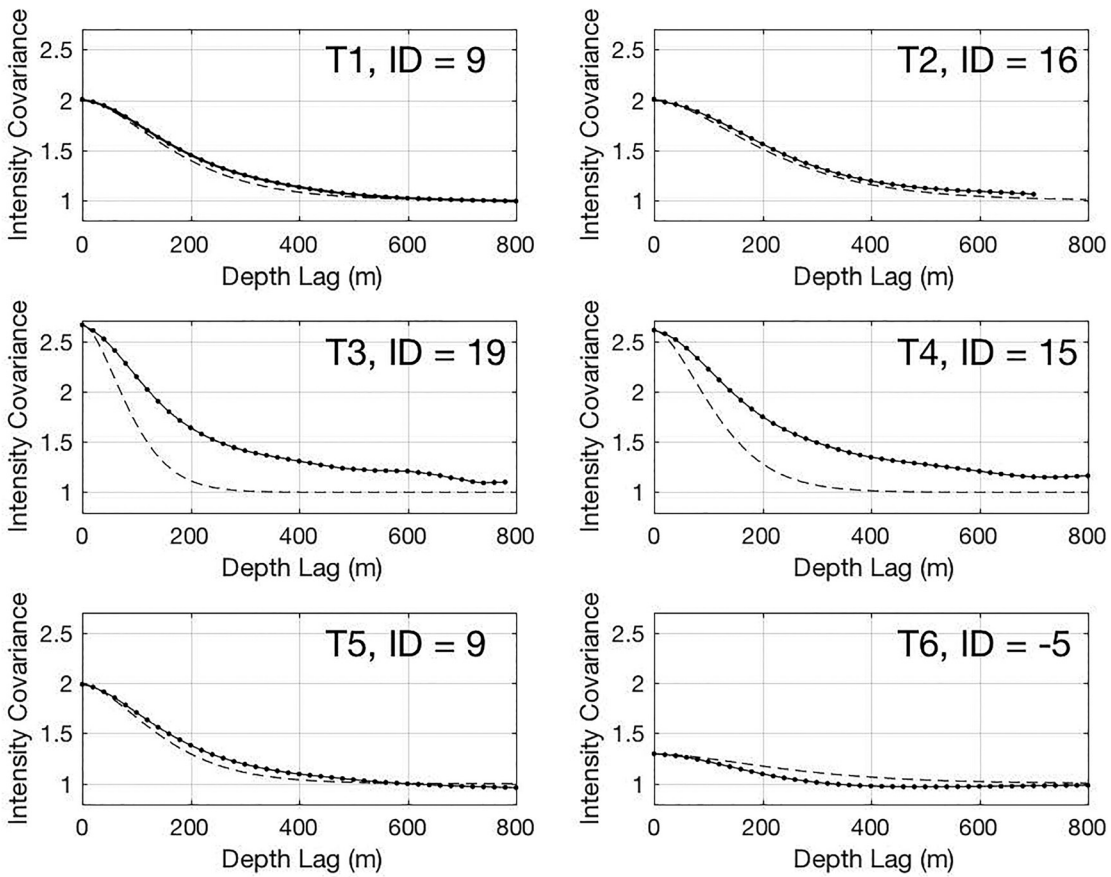

FIG. 11. Observed (dotted) and modeled (dash), vertical intensity covariance functions for the six ray paths. Vertical intensity correlation lengths defined as the $1 + SIe^{-1/2}$ crossing point of the functions are given in Table III.

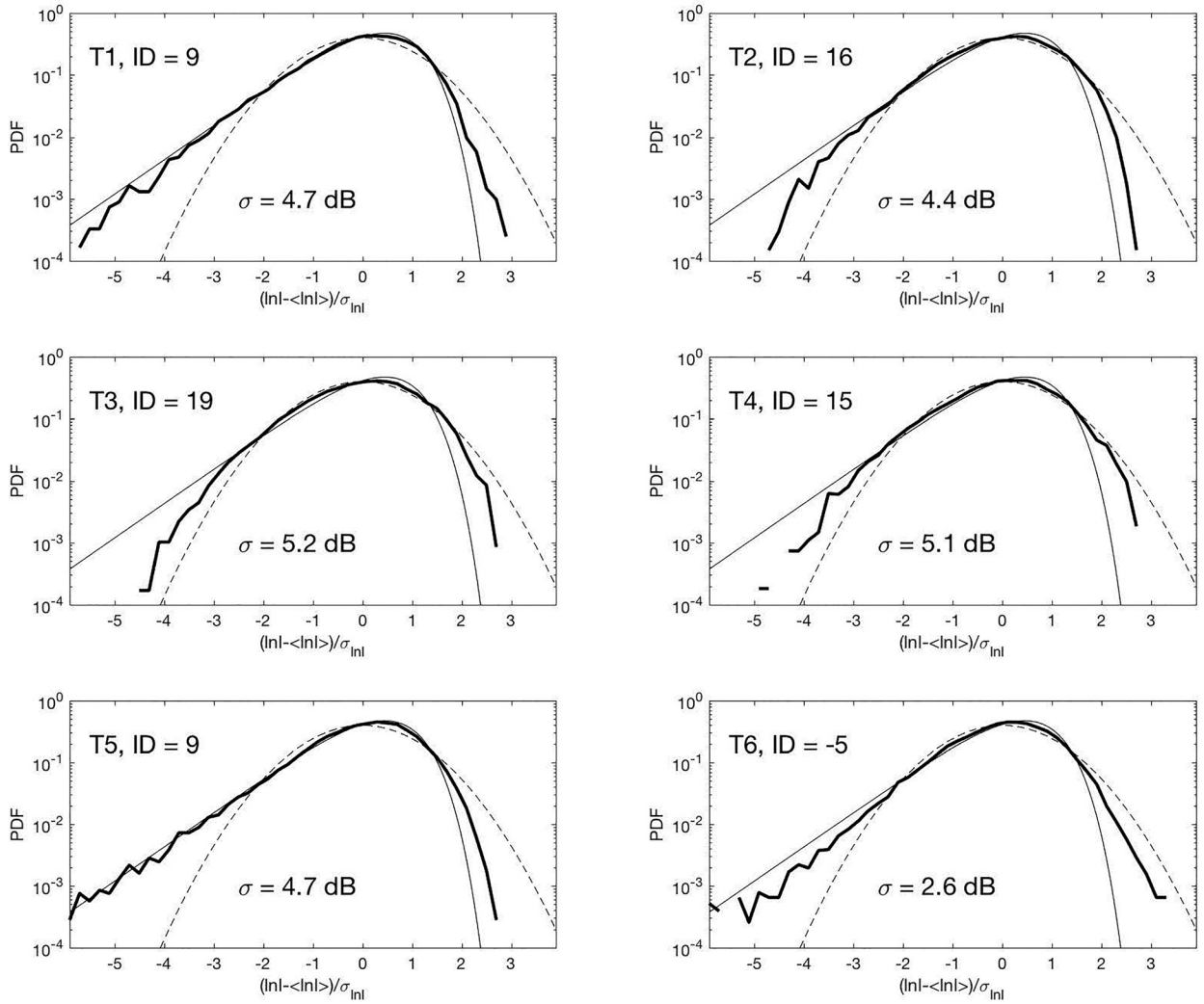

FIG. 12. Observed log-intensity PDFs for the six ray paths (bold). Model PDFs are log-normal (dashed) and exponential (solid).

the mean value (Fig. 13). For these strongly scintillating paths (T3 and T4), a modulated exponential PDF (Colosi *et al.*, 2001) compares favorably with the observations, reproducing both the heavy tail and the curvature at smaller values of $I/\langle I\rangle$. The physical picture of the modulated exponential is a saturated microray interference in accord with the central limit theorem for which $SI = 1$, but the ray tubes of these groups of rays are modulated by the large-scale ocean structure, giving $SI > 1$. The T1, T2, and T5 paths are all similar, showing exponential PDF behavior at high intensity but deviations from the models at low intensity. As expected, the weakly varying T6 path bears no resemblance to the exponential PDF.

V. DISCUSSION

In Secs. III and IV, various measures of the variability of phase and intensity were described for six ray paths that have similar vertical sampling properties, but different frequencies and ranges. It was also shown that path integral theory with a simple GM model of the ocean fine structure was able to adequately reproduce the experimental results within a factor of two but typically much better. These results raise some interesting questions that bear further examination.

A. Wave propagation regimes: Λ – Φ

An important issue is whether the signal statistics can be characterized using the unsaturated, partially saturated, and fully saturated propagation regimes as predicted for the Philippine Sea observations using Λ – Φ theory (Colosi, 2015, 2016). Briefly, this theory uses two parameters, the rms phase Φ and a diffraction parameter Λ, which are a weighted average of the vertical Fresnel zone divided by an ocean vertical scale (Appendix A). The three propagation regimes can be mapped out in Λ – Φ space using an empirical equation relating Φ and Λ to the variance of log-intensity, i.e.,

$$\sigma^2_{\ln I} \simeq \Lambda\Phi^2\left[\left(\frac{1}{\pi} - 0.1\right)e^{-\Lambda/1.5} + 0.1\right], \tag{12}$$

and a microray interference condition $\Phi\Lambda = 1$.

Computing the parameters for the six ray paths analyzed here gives the predictions shown in Fig. 14. The T1 path is predicted to be in the partially saturated regime, the T5 path is predicted to be on the border between the unsaturated and

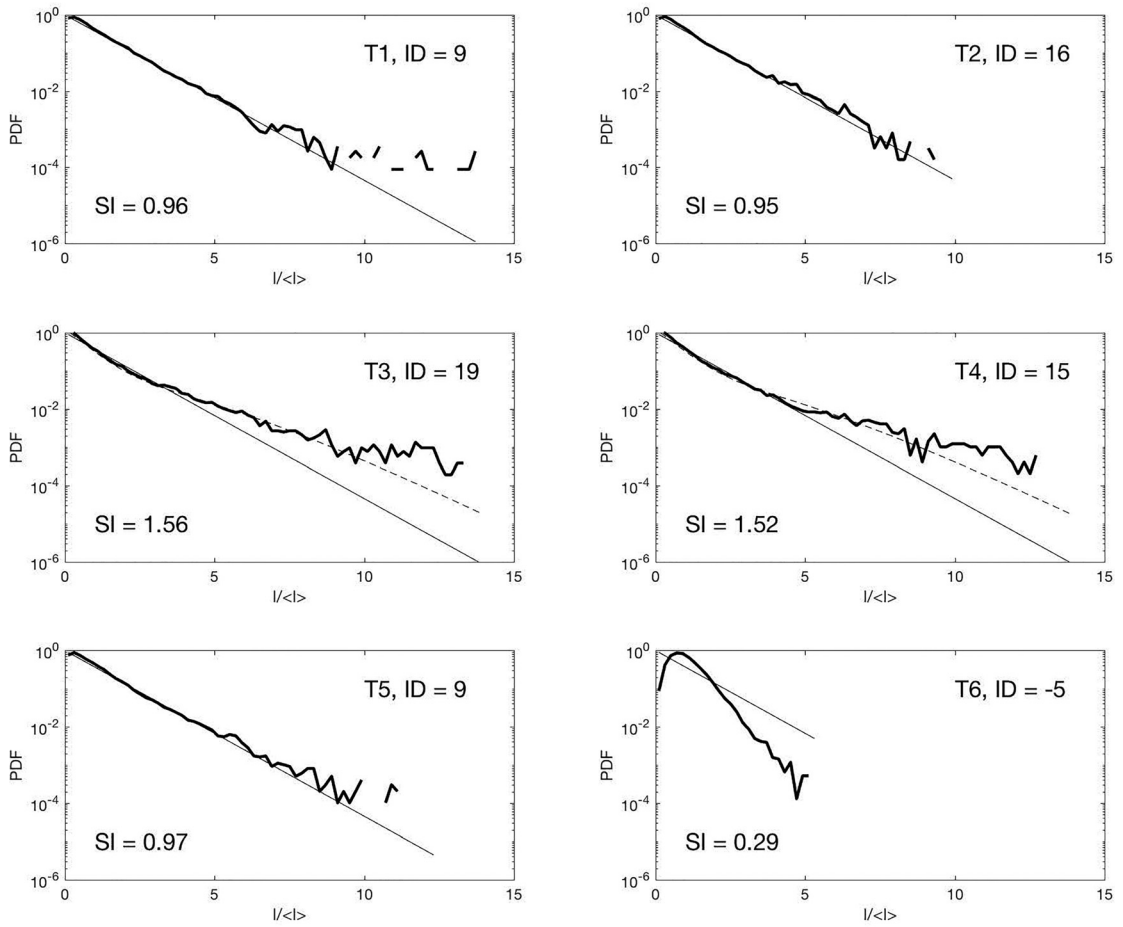

FIG. 13. Observed intensity PDFs for the six ray paths (bold). Model PDFs are exponential (solid) and modulated exponential (dashed, only middle panels).

partially saturated regimes, and the T6 path is predicted to be solidly in the unsaturated regime. The more strongly variable paths T2, T3, and T4 are predicted to be in the saturated regime, but they, along with T1, are in a rather ambiguous region of the diagram where the partially saturated regime is shrinking. Plotting the scintillation indices vs range (Fig. 14, lower panel) is helpful. From the PDFs (Figs. 12 and 13), it is apparent that T6 and T5 are properly placed on the diagram. Given the close similarity between signal statistics at T1 and T5, T1 should be considered to be on the border between the unsaturated and partially saturated regimes. Because the diffraction parameter for T2 is large and clearly separated from the higher frequency observations on the scintillation index plots, it may in fact be in the proper regime on the border between unsaturated and saturated. More ranges at this lower frequency would be needed to remove the ambiguity. The most strongly fluctuating paths T3 and T4 have large scintillation indices and moderate log-intensity variances and they should therefore be in the partially saturated regime. The estimated propagation regimes are given in Table III.

Further physical insight into the propagation can be obtained using the $\Lambda - \Phi$ diagram. The observations give estimates of Φ and $\sigma^2_{\ln I}$ and an effective observed diffraction parameter, Λ_{obs}, can therefore be calculated using Eq. (12). It is seen that the observations are behaving less diffractively than the theory estimates (Fig. 14), although Eq. (12) is based on weak fluctuation theory and not expected to be as accurate for the more strongly fluctuating paths, T3 and T4. The weaker diffraction could be due to two factors, one oceanographic and one acoustical. The oceanographic case would be if the small-scale ocean sound-speed structure differs significantly from the GM model. Here, the relevant small-scale structure is at vertical scales equal to and less than the Fresnel zone. On the acoustical side, the Fresnel zone is a narrowband construct, and the observations here have significant bandwidths relative to the center frequencies. For broadband transmissions, the effective Fresnel zone is expected to be smaller than the narrowband result, although the problem is not well understood (Colosi, 1999). This issue could be resolved using Monte Carlo numerical simulations.

B. Phase structure function

The observations of vertical coherence and intensity covariance are, according to path integral theory, driven by the phase structure function. It is therefore instructive, given the good agreement between observation and theory, to use the observations to directly examine the phase structure function. One could do this in two ways. The most direct method would be to use the phases along the front (Fig. 4) and compute the structure functions from these unwrapped phases. This method is problematic, however, due to

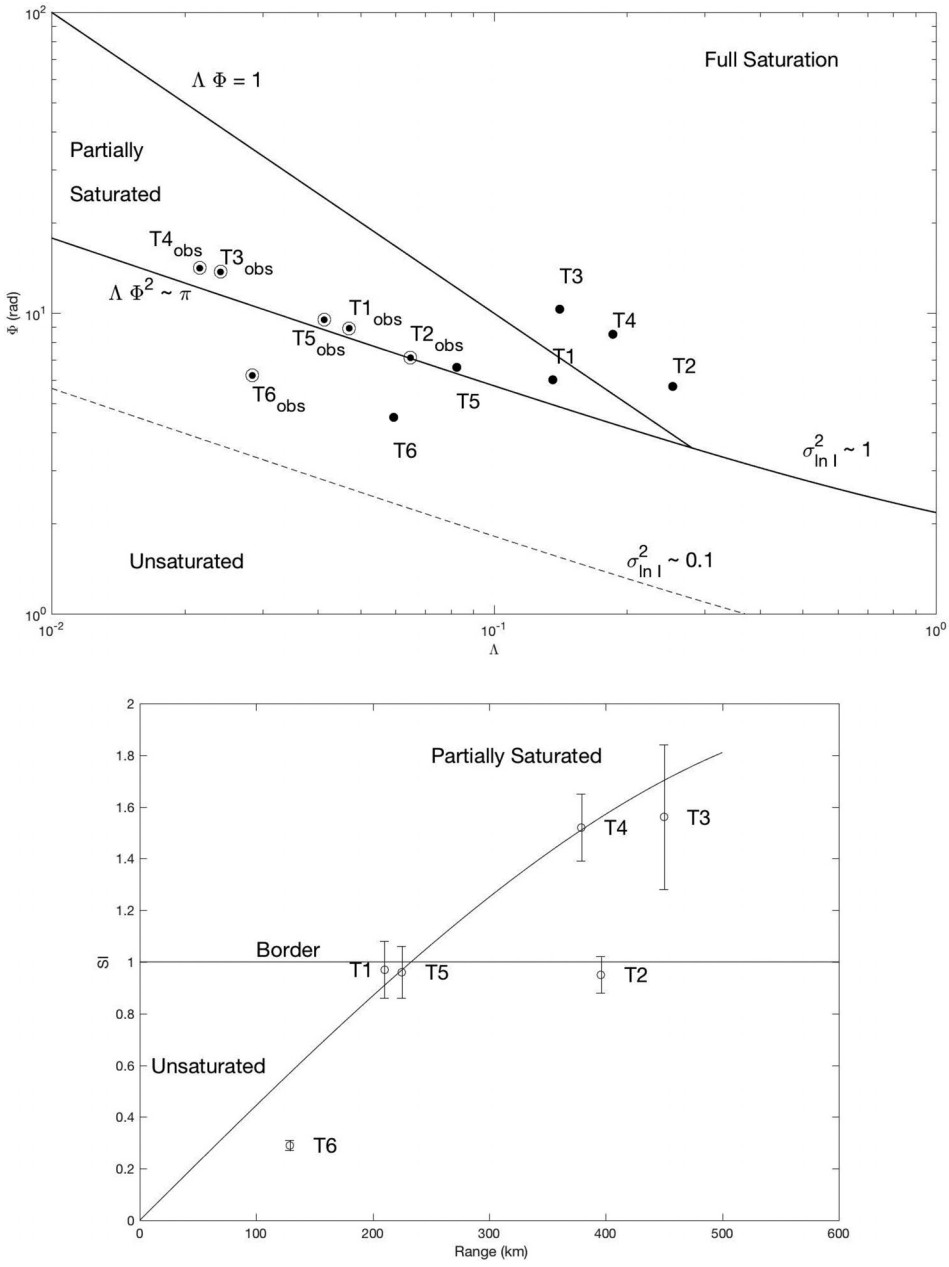

FIG. 14. $\Lambda - \Phi$ diagram for the ray paths analyzed here (upper) and observed scintillation index vs range (lower). Predictions of Λ and Φ for all six paths are shown with dots and labeled by source. The observed values of Φ and $\sigma^2_{\ln I}$ can be used to estimate an effective observed Λ value using Eq. (12). The points based on the observations are shown with circled dots.

fadeouts where the phase cannot be adequately tracked. A second method, which is adopted here, is to use the path integral equations and invert the observations to get the structure function. Using vertical coherence, and removing the frequency dependence one can write

$$D(\Delta z_r) = -\frac{2\ln|\langle pp^*(\Delta z_r)\rangle|}{\omega_c^2}. \tag{13}$$

The resulting structure function is a travel time structure function. Similarly, using the intensity covariance, the result is

$$D(\Delta z_r) = -\frac{1}{\omega_c^2}\ln\left(\frac{\langle I(\Delta z_r)I\rangle - 1}{SI}\right). \tag{14}$$

The structure functions so obtained, as well as the theoretical prediction from Eq. (4), are plotted in log-log form in Fig. 15. The nearly linear form for all of the paths implies a power law relation,

$$D(\Delta z_r) \propto (\Delta z_r)^p, \tag{15}$$

where the least square fit exponents are also shown in the figure. The theory gives exponents in a rather narrow range, $1.54 < p < 1.65$, for the six paths. This indicates why the quadratic approximation ($p = 2$) that is commonly used is inaccurate in this case.[3] The intensity covariance exponents are also in a relatively narrow range and in agreement with the theory, $1.49 < p < 1.59$, except for path T6 with $p = 1.82$. The exponents estimated from the vertical coherence, on the other hand, vary widely and unsystematically, $1.19 < p < 1.55$. These values are generally smaller than those from the theory and the intensity covariance. This result is understandable since the coherence function estimates are sensitive to phase errors associated with mooring motion and alignment of the time front.

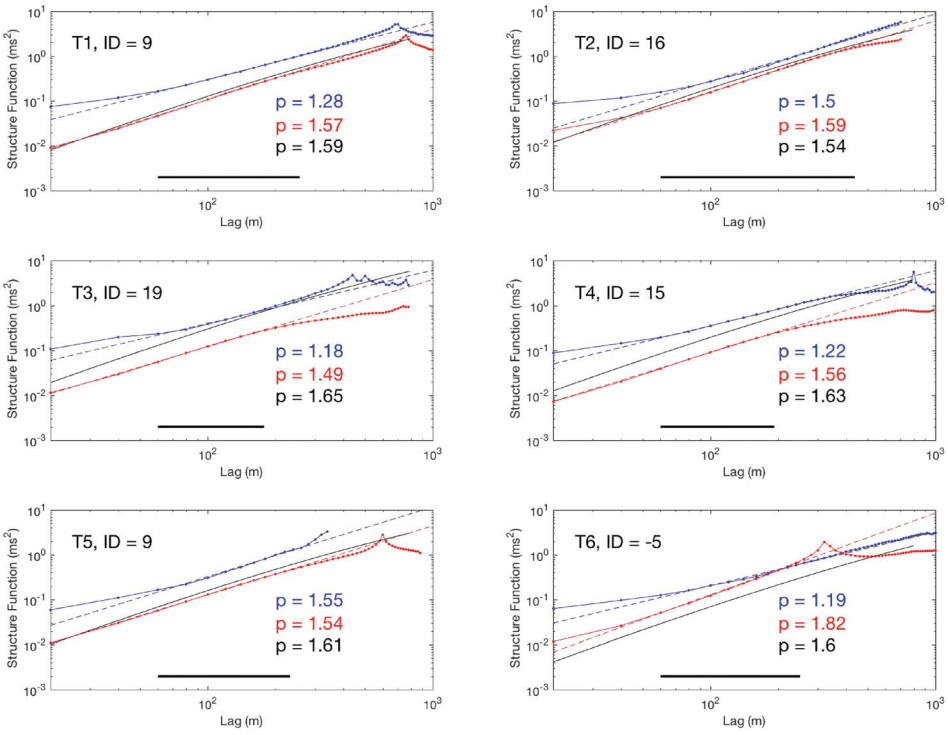

FIG. 15. Phase structure function estimated from vertical coherence (blue), vertical intensity covariance (red), and theory (black). The p values give the power law dependence on lag, estimated by linear least square fits (dashed, fit not shown for the theory). The lag region over which the fit is made is shown at the bottom of the plots (horizontal bold line).

The agreement between the theory and the intensity covariance is therefore all the more favorable. It should also be noted that the power law behavior of the structure function has implications for the range scaling of the coherence. Because $D_{12} \propto R$, the coherence length z_0 goes as $R^{1/p}$.[3]

C. Glint and fade-out rates

A final topic that has practical implications for communication and detection applications are the glint and fade-out rates. These rates are defined as the number of events exceeding a certain threshold that one would expect per unit time and hydrophone number. While eight observation per day every other day do not give detailed time evolution information, glint and fade statistics can be derived as follows. Each pulse reception is the result of a 135-s duration FM sweep. Therefore, if N_g and N_f glints and fades are observed over N_t total receptions and over N_h hydrophones, then the glint and fade-out rates per phone will be

$$R_g = \frac{N_g}{135 N_t N_h}, \quad R_d = \frac{N_f}{135 N_t N_h}. \tag{16}$$

The assumption is that the glint/fadeout rate is less than the sample rate (e.g., 1/135 s). Here, we are not concerned with the duration of the glints or fade-outs only that one is observed over the 135-s FM sweep. These rates are displayed in Table III, columns 7 and 8, where the glint and fade-out thresholds are $+6$ dB and -10 dB relative to the mean intensity. For all paths except for T6, a five phone array observes several glint and fade-out events per hour. As expected, the longest ranges have the largest rates (T3 and T4). In addition, the T2 and T4 paths show roughly a linear scaling with frequency, and the nearly identical paths T1 and T5 have close values.

The fade-out rate R_d is interpretable in terms of the coherence time of the channel and multipath interference (Dyson *et al.*, 1976). Accordingly, for a fade-out threshold of $F = 10 \log_{10}(\epsilon^{-1})$ dB, the time between fade-outs is

$$T_f = \frac{t_0 \pi^{3/2}}{2\epsilon}, \tag{17}$$

where t_0 is the coherence time ($e^{-1/2}$ point). The observation is $R_d \times 1\text{phone} = 1/T_f$ and therefore the fade-out rate suggests a coherence time of

$$t_0 \simeq \frac{2\epsilon}{\pi^{3/2} R_d}. \tag{18}$$

For a 10-dB fade-out, $\epsilon \simeq 0.316$, and R_d is of order 1 for paths 1 to 5, so $t_0 \simeq 6.8$ min. For the six paths T1 to T6 the path integral estimates of t_0 using the quadratic approximation to the structure function (see Appendix A) are 6.0, 6.9, 3.9, 4.3, 5.9, and 9.6 min, respectively. Using these theoretical coherence times, predicted values of R_d can be calculated. Except for path T6, which is in the unsaturated regime (weak or no multipath interference), the comparisons are favorable (Table III).

VI. SUMMARY AND CONCLUSIONS

Using year-long observations from the Philippine Sea, phase and intensity statistics have been quantified along six similar acoustic ray paths that have upper turning points in the mid-thermocline. While the paths are similar in their vertical sampling properties, they are along different azimuths and at different ranges (129–450 km) within the pentagonal array. Also, five of the six ray paths have similar center frequencies (250–275 Hz), while the sixth ray path has a much lower center frequency of 172.5 Hz. Acoustic observables

quantified include variances of phase and intensity, vertical mutual coherence functions, vertical covariance of intensity, intensity PDFs, and fadeout and glint rates. Key results are summarized as follows.

First, scaling several of the statistics for range and frequency shows that the observed variability in the internal-wave band is very nearly horizontally isotropic, i.e., there are no distinct differences in the high-frequency fluctuations along the different azimuths. However, examining phase fluctuations in the tidal and sub-inertial/mesoscale bands, strong anisotropy is observed due to the directionality of the internal tide and the inhomogeneity of the eddy field. For intensity fluctuations, the variability is dominated by stochastic internal wave scale processes, and there is no observed modulation at either tidal or sub-inertial frequencies (White *et al.*, 2016).

Second, guided by *in situ* observations of internal waves, path integral predictions using the GM spectrum for rms phase, vertical mutual coherence function, and vertical intensity covariance show agreement with the observations to well within a factor of two. This level of agreement should be considered acceptable given the number of assumptions in the theory, including the GM spectral form. The agreements with the path integral results for these two vertically-lagged functions allow an analysis of the phase structure function. The structure function was found to obey a power law, $D \propto \Delta z_r^p$. The path integral theory and the intensity covariance observations are in close agreement, giving a power law exponent of $p \simeq 1.5$. The vertical mutual coherence results are more variable, likely due to phase errors that affect the coherence and not the intensity covariance.

Moments of phase and intensity, along with PDFs of intensity, shed light on the propagation regimes of unsaturated, partially saturated, and fully saturated wave fields. The observations reveal propagation behavior typical of the unsaturated regime, the border of the unsaturated and partially saturated regimes, and strong focusing associated with the partially saturated regime. Using the $\Lambda - \Phi$ method, the propagation regimes for the shorter range paths and the low-frequency path are adequately predicted (T1, T2, T5, and T6), but the longer range paths (T3 and T4) are inaccurately predicted to be in the fully saturated regime. Using the observations of rms phase and variance of log-intensity, an effective diffraction parameter Λ can be estimated that properly relocates the six paths on the diagram. The "observed" Λ is smaller than the theoretical one, suggesting that the propagation is less diffractive, perhaps due to differences in the small-scale ocean structure near the Fresnel zone scale, or to the use of the Fresnel zone itself, which is a narrowband concept.

Even though the sample rate in the experiment was eight transmissions per day every other day, fade-out and glint rates were estimated, giving a small view into the time behavior of the signals. Using thresholds of +6 dB and −10 dB for glints and fades, it is found that with the exception of the shortest path, T6, a modest five-phone array would see several glints and fades per hour. The fade-out rate can be interpreted in terms of the signal coherence time, t_0, assuming a multipath interference pattern. Estimates of coherence time based on the fade-out rate are in good agreement with those from path integral theory.

The results of this study suggest a reasonable understanding of the propagation physics for this set of six ray paths that traverse the mid-thermocline. Within the scope of the Philippine Sea data set, the next challenge is to see if similar results can be obtained for more axial propagation or more upper-ocean propagation. From the path integral standpoint, the more axial paths have smaller errors due to the ray tangent approximation. In addition, the near-axial sound-speed perturbations will be dominated by GM-like internal waves with little contribution from spicy structures. On the other hand, the higher angle paths going into the upper ocean will have greater ray tangent approximation errors and will be sampling regions of higher spice as well as regions where the GM model is expected to be less accurate.

An important topic not treated in this paper is the observable of pulse time spread, which is related to the cross frequency MCF. Time spread is important because it reveals the effects of microray interference, a process considered responsible for intensity fluctuations. It has been found that several hundreds of Hertz transmissions to the DVLA at 510-km range show little time spread within 3 dB of the peak (Andrew *et al.*, 2016) and that this is consistent with approximate pulse spread estimates, τ_0, from path integral theory (Colosi, 2016). The observation of small pulse spread near the peak is also evident from the mean pulses computed in the present work (Fig. 3). However, this study (Andrew *et al.*, 2016) is limited in the sense that pulse spread was estimated by wander-corrected ensemble average pulses (such as in Fig. 3), instead of the wander insensitive time-lagged intensity covariance. A more direct analysis is therefore needed with a focus not just on pulse shape variations near the peak but on those in the tails. In terms of the theory, it is also important to account for high angle ray geometry and to use full solutions of the quadratic path integral for the frequency MCF instead of the quadratic approximation giving rise to the τ_0 value. This analysis is beyond the scope of the present manuscript.

ACKNOWLEDGMENTS

This work was supported by the Office of Naval Research.

APPENDIX A: INTERNAL WAVE SPECTRAL REPRESENTATION

The ocean sound-speed field is assumed to be of the form

$$c_{tot}(\mathbf{r}, t) = c(z) + \delta c(\mathbf{r}, t), \tag{A1}$$

where $c(z)$ is the background sound speed and $\delta c(\mathbf{r}, t)$ is a perturbation due to internal waves. The strength of the perturbations varies with depth according to the WKB result

$$\langle \delta c^2 \rangle = \zeta_0^2 \frac{N_0}{N(z)} \left(\frac{dc(z)}{dz} \right)_p^2, \tag{A2}$$

where ζ_0 is a reference displacement and $N_0 = 3$ cph is a reference buoyancy frequency.

The GM internal wave spectrum in terms of frequency σ and vertical mode number j is given by

$$F_\zeta(\sigma,j) = \zeta_0^2 \frac{N_0}{N(z)} B(\sigma) H(j) \tag{A3}$$

$$B(\sigma) = \frac{4}{\pi} \frac{\sqrt{\sigma^2 - f^2}}{\sigma^3} \tag{A4}$$

$$H(j) = \frac{1}{N_j} \frac{1}{j^2 + j_*^2}, \tag{A5}$$

where f is the Coriolis frequency, $f \le \sigma \le N(z)$, $1 \le j \le J$, and N_j gives a unit normalization. The modal bandwidth parameter, j_*, is taken to be 3. The maximum vertical mode number, J, is obtained by requiring a Richardson number of unity, giving the result

$$J = \frac{(N_0 B)^2}{6\pi \zeta_0^2 N_0^2 j_*}, \tag{A6}$$

where $N_0 B = \int_0^D N(z) dz$. In this study, we have $N_0 B = 9.37$ rad m/s, and $\zeta_0 = 10.17$ m, which gives $J = 548$.

APPENDIX B: PATH INTEGRAL EXPRESSIONS

Several explicit path integral expressions using the GM spectrum are given here for completeness (see Colosi, 2016, for more details). In the ray tangent approximation, the correlation length of the internal waves in the local direction of the ray (θ) is given by

$$L_p(z,\theta) = \langle j^{-1} \rangle \frac{4}{\pi^2} \frac{N_0 B}{f} \left(\frac{1}{1+a^2} + \frac{a^2}{2} \frac{1}{(1+a^2)^{3/2}} \times \ln\left(\frac{(1+a^2)^{1/2}+1}{(1+a^2)^{1/2}-1} \right) \right), \tag{B1}$$

where $a = N(z)\tan\theta/f$. Some important mode spectral averages are

$$\langle j^{-1} \rangle = \sum_{j=1}^{J} \frac{H(j)}{j} \quad \text{and} \quad \langle j \rangle = \sum_{j=1}^{J} j H(j). \tag{B2}$$

The mean square phase and diffraction parameter are

$$\Phi^2 = \omega_c^2 \int_\Gamma ds \, \frac{\langle \mu^2(z) \rangle L_p(\theta, z)}{c^2(z)}, \tag{B3}$$

$$\Lambda = \frac{\omega_c^2}{\Phi^2} \int_\Gamma ds \, \frac{\langle \mu^2(z) \rangle L_p(\theta, z)}{c^2(z)} \frac{\{m^2\} R_f^2(s)}{2\pi}, \tag{B4}$$

with

$$\{m^2\} = \frac{1}{\langle j^{-1} \rangle} \sum_{j=1}^{J} \frac{H(j)}{j} m^2(j) = \left(\frac{\pi N(z)}{N_0 B} \right)^2 \frac{\langle j \rangle}{\langle j^{-1} \rangle}, \tag{B5}$$

where the last step follows using the WKB vertical wave number $m(j) = \pi j N(z)/N_0 B$. The fractional sound-speed variance is given by $\langle \mu^2(z) \rangle = \langle \delta c^2(z) \rangle / c^2(z)$, and $R_f(s)$ is the vertical Fresnel zone scale.

In the quadratic approximation to the time-lagged phase structure function, the result is $D(\Delta t) = \Delta t^2 / t_0^2$, with the time coherence given by

$$\frac{1}{t_0^2} = \omega_c^2 \int_\Gamma ds \frac{\langle \mu^2(s) \rangle L_p(s)}{c^2(z)} \{\sigma^2\}. \tag{B6}$$

The spectral average of the internal wave frequency σ^2 is

$$\{\sigma^2\} = M_\sigma \int_{\sigma_L}^{N} d\sigma \, \frac{\sigma_L^2}{\sigma} \left(\frac{\sigma^2 - f^2}{\sigma^2 - \sigma_L^2} \right)^{1/2} = \frac{M_\sigma \sigma_L^2}{2} \left[\ln\left(\frac{2N^2 - \sigma_L^2 - f^2 + 2(N^2 - \sigma_L^2)^{1/2}(N^2 - f^2)^{1/2}}{\sigma_L^2 - f^2} \right) + \frac{f}{\sigma_L} \ln\left(\frac{N^2(\sigma_L^2 + f^2) - 2f^2\sigma_L^2 - 2f\sigma_L(N^2 - \sigma_L^2)^{1/2}(N^2 - f^2)^{1/2}}{N^2(\sigma_L^2 - f^2)} \right) \right], \tag{B7}$$

where the normalization factor is

$$M_\sigma^{-1} = \int_{\sigma_L}^{N} d\sigma \frac{\sigma_L^2}{\sigma^3} \left(\frac{\sigma^2 - f^2}{\sigma^2 - \sigma_L^2} \right)^{1/2} = \frac{1}{2} \left[\left(1 - \frac{\sigma_L^2}{N^2} \right)^{1/2} \left(1 - \frac{f^2}{N^2} \right)^{1/2} + \left(\frac{\sigma_L}{f} - \frac{f}{\sigma_L} \right) \times \ln\left(\frac{(f/\sigma_L)(1 - \sigma_L^2/N^2)^{1/2} + (1 - f^2/N^2)^{1/2}}{(1 - f^2/\sigma_L^2)^{1/2}} \right) \right], \tag{B8}$$

and $\sigma_L^2 = f^2 + N^2 \tan^2\theta$.

APPENDIX C: RAY TUBE FUNCTIONS

Ray tube functions give information concerning the behavior of closely spaced rays and are traditionally evaluated using ray tube equations (Esswein and Flatté, 1981) or variational equations (Colosi, 2015). These methods both require knowledge of the background sound-speed profile curvature, which is difficult to obtain from experimental profiles. A way around this problem is to work with the ray tube functions, ξ_1 and ξ_2, that are defined in the vicinity of an eigenray $z_r(x)$. The boundary conditions on these functions at the source ($x = 0$) and receiver ($x = R$) are

$$\xi_1(x=0)=0, \quad \xi_1(x=R)=1 \quad \text{and}$$
$$\xi_2(x=0)=1, \quad \xi_2(x=R)=0. \tag{C1}$$

Physically, ξ_1 describes the path of a ray starting at the source and ending a unit vertical distance away at the receiver, while ξ_2 describes the path of a ray starting at the receiver and ending a unit vertical distance away at the source (Colosi, 2016). The numerical recipe for computing ξ_1 is therefore (1) find an eigenray, $z_r(x)$, and its launch angle θ_0, (2) trace a new ray starting at the source with a slightly different launch angle from the eigenray (typically $\delta\theta_0 \simeq 10^{-5}$ radians), call it $\hat{z}_1(x)$, and (3) form the ray tube function using $\xi_1(x) = (z_r(x) - \hat{z}_1(x))/(z_r(R) - \hat{z}_1(R))$. Similarly, in order to find ξ_2, use the eigenray $z_r(x)$, but now trace the new ray starting at the receiver headed back towards the source, but starting with a slightly different launch angle than the received angle. Call this backwards going ray $\hat{z}_2(x)$. The second ray tube function is $\xi_2(x) = (z_r(x) - \hat{z}_2(x))/(z_r(R) - \hat{z}_2(R))$, and the required ray tube functions have been obtained without using a sound-speed second derivative. Note, however, that a numerical derivative of the ray path with respect to the initial angle is being carried out, and some care must be taken to ensure numerical accuracy.

These ray tube equations can be used to estimate the vertical separation between two nearby rays for use in the vertical phase structure function calculation, that is

$$\Delta z(x) = \xi_1(x)\Delta z_r, \tag{C2}$$

where Δz_r is the ray separation at the final range. In addition, the functions are used to compute the vertical Fresnel zone given by

$$R_f^2(x) = \frac{\lambda\xi_1(x)\xi_2(x)}{\xi_1\partial\xi_2 - \xi_2\partial_x\xi_1}, \tag{C3}$$

where λ is the wavelength of the sound. The denominator in the Fresnel zone equation, called the Wronskian, is a constant along the path and so can be evaluated at any x value (Colosi, 2016).

[1]A separate analysis of the same moored CTD data presented here was done to estimate internal-wave spectra and energy levels (Andrew *et al.*, 2016). That study estimated the GM energy level to be 0.9, which is considerably lower than the present estimate of 1.94. This difference can be attributed to methodology. In their work, internal wave displacements are estimated using sound speed not potential density, and thus sound-speed spectral levels are converted to vertical displacement using an average vertically-smoothed potential sound speed gradient profile. This approach has two drawbacks, which call the energy level estimate into question. First, working with sound speed instead of potential density does not separate spice and internal waves properly. Second, the GM energy level is sensitive to the assumed averaged smoothed potential sound-speed gradient. No such sensitivity is in the present analysis using potential density because isopycnal depths are obtained at each measurement time using vertical interpolation.

[2]The exponential distribution is the intensity PDF one obtains via the Central Limit Theorem when the complex pressure is the sum of many independent contributions.

[3]The $p=2$ case is when the structure function is approximated as a quadratic function of lag, such as in Eq. (5).

Andrew, R., Ganse, K., White, A., Mercer, J., Worcester, P., Dzieciuch, M., and Colosi, J. (**2016**). "Low-frequency pulse propagation over 510 km in the philippine sea: A comparison of observed and theoretical pulse spreading," J. Acoust. Soc. Am. **140**, 216–228.

Brekhovskikh, L. (**1949**). "Concerning the propagation of sound in an underwater acoustic channel," Dokl. Akad. Nauk SSSR **69**, 157–160.

Colosi, J. (**1999**). "A review of recent results on ocean acoustic wave propagation in random media: Basin scales," IEEE J. Ocean. Eng. **24**, 138–155.

Colosi, J. (**2013**). "On horizontal coherence estimates from path integral theory for sound propagation through random ocean sound-speed perturbations," J. Acoust. Soc. Am. **134**, 3116–3118.

Colosi, J. (**2015**). "A re-formulation of the Λ-Φ diagram for the prediction of ocean acoustic fluctuation regimes," J. Acoust. Soc. Am. **137**(5), 2485–2494.

Colosi, J. (**2016**). *Sound Propagation through the Stochastic Ocean* (Cambridge University Press, Cambridge, UK), p. 420.

Colosi, J., Duda, T., Lin, T., Lynch, J., Newhall, A., and Cornuelle, B. (**2012**). "Observations of sound speed fluctuations on the New Jersey continental shelf in the summer of 2006," J. Acoust. Soc. Am. **131**(2) 1733–1748.

Colosi, J., Tappert, F., and Dzieciuch, M. (**2001**). "Further analysis of intensity fluctuations from a 3252-km acoustic propagation experiment in the eastern North Pacific Ocean," J. Acoust. Soc. Am. **110**, 163–169.

Colosi, J., Van Uffelen, L., Cornuelle, B., Dzieciuch, M., Worcester, P., Dushaw, B., and Ramp, S. (**2013**). "Observations of sound speed fluctuations in the western Philippine Sea in the spring of 2009," J. Acoust. Soc. Am. **134**, 3185–3200.

Dashen, R., Flatté, S., and Reynolds, S. (**1985**). "Path-integral treatment of acoustic mutual coherence functions for rays in a sound channel," J. Acoust. Soc. Am. **77**, 1716–1722.

DiMaggio, D., Colosi, J., Joseph, J., Pearson, A., Worcester, P., and Dzieciuch, M. (**2018**). "Observations of thermohaline sound-speed structure induced by internal waves and spice in the summer 2015 Canada basin marginal ice zone," Elementa Sci Anth. **6**(1), 30.

Dozier, L., and Tappert, F. (**1978**). "Statistics of normal-mode amplitudes in a random ocean. I. Theory," J. Acoust. Soc. Am. **63**, 353–365.

Duda, F. T., and Bowlin, J. (**1994**). "Ray-acoustic caustic formation and timing effects from ocean sound speed relative curvature," J. Acoust. Soc. Am. **96**, 1033–1046.

Duda, T., Flatte, S., Colosi, J., Cornuelle, B., Hildebrand, J., Hodgkiss, B., Worcester, P., Howe, B., Mercer, J., and Spindel, R. (**1992**). "Measured wave-front fluctuations in 1000-km pulse propagation in the Pacific Ocean," J. Acoust. Soc. Am. **92**, 939–955.

Dyson, F., Munk, W., and Zetler, B. (**1976**). "Interpretation of multi path scintillations Eleuthera to Bermuda in terms of internal waves and tides," J. Acoust. Soc. Am. **59**, 1121–1133.

Dzieciuch, M. (**2014**). "Signal processing and tracking of arrivals in ocean acoustic tomography," J. Acoust. Soc. Am. **136**, 2512–2536.

Eckart, C., and Carhart, R. (**1950**). "Fluctuation of sound in the sea," in *Basic Problems in Underwater Acoustics* (Committee on undersea warfare, National Research Council, Washington, DC), pp. 63–122.

Esswein, R., and Flatté, S. (**1981**). "Calculation of the phase structure function density from oceanic internal waves," J. Acoust. Soc. Am. **70**, 1387–1396.

Ewing, M., and Worzel, J. (**1948**). "Long-range sound transmission," Geol. Soc. Am. Memoirs **27**, 1–32.

Flatté, S. (**1983**). "Wave propagation through random media: Contributions from ocean acoustics," Proc. IEEE **71**, 1267–1294.

Flatté, S., Dashen, R., Munk, W., Watson, K., and Zachariasen, F. (**1979**). *Sound Transmission Through a Fluctuating Ocean* (Cambridge University Press, Cambridge, UK), p. 299.

Flatté, S., Reynolds, S., and Dashen, R. (**1987**). "Path-integral treatment of intensity behavior for rays in a sound channel," J. Acoust. Soc. Am. **82**, 973–981.

Flatté, S., and Rovner, G. (**2000**). "Calculation of internal-wave induced fluctuations in ocean acoustic propagation," J. Acoust. Soc. Am. **108**(2), 526–534.

Garrett, C. J., and Munk, W. H. (**1972**). "Space-time scales of internal waves," Geophys. Fluid Dyn. **2**, 255–264.

Kerry, C., Powell, B., and Carter, G. (**2013**). "Effects of remote generation sites on the model estimates of M2 internal tides in the Philippine Sea," J. Phys. Ocean. **43**, 187–204.

Levine, M. D. (**2002**). "A modification of the Garrett-Munk internal wave spectrum," J. Phys. Ocean. **32**, 3166–3181.

Munk, W., Worcester, P., and Wunsch, C. (**1995**). *Ocean Acoustic Tomography* (Cambridge University Press, Cambridge, UK), p. 433.

Munk, W., and Zachariasen, F. (**1976**). "Sound propagation through a fluctuating stratified ocean: Theory and observation," J. Acoust. Soc. Am. **59**, 818–838.

Powell, B., Kerry, C., and Cornuelle, B. (**2013**). "Using a numerical model to understand the connection between the ocean and acoustic travel-time measurements," J. Acoust. Soc. Am. **134**, 3211–3222.
Ramp, S., Colosi, J., Worcester, P., Bahr, F., Heaney, K., Mercer, J., and VanUffelen, L. (**2017**). "Eddy properties in the subtropical countercurrent, Western Philippine Sea," Deep Sea Res. **125**, 11–25.
Uscinski, B. (**1982**). "Intensity fluctuations in a multiple scattering medium. Solution of the fourth moment equation," Proc. R. Soc. London Ser. A **380**, 137–169.
White, A., Henyey, F., Andrew, R., Mercer, J., Worcester, P., Dzieciuch, M., and Colosi, J. (**2016**). "Internal tides and deep diel fades in acoustic intensity," J. Acoust. Soc. Am. **140**, 3952–3962.
Worcester, P. F., Dzieciuch, M. A., Mercer, J. A., Andrew, R. K., Dushaw, B. D., Baggeroer, A. B., Heaney, K. D., Gerald, L., Colosi, J. A., Stephen, R. A., Kemp, J. N., Howe, B. M., Van Uffelen, L. J., and Wage, K. E. (**2013**). "The North Pacific acoustic laboratory deep-water acoustic propagation experiments in the Philippine Sea," J. Acoust. Soc. Am. **134**(4), 3359–3375.